

2016

Carbon Nanotube Thin Film Supported by Nickel Nanotube Array as Supercapacitor Electrode with Improved Rate Capability

Hosein Monshat
Iowa State University

Follow this and additional works at: <https://lib.dr.iastate.edu/etd>

 Part of the [Mechanical Engineering Commons](#)

Recommended Citation

Monshat, Hosein, "Carbon Nanotube Thin Film Supported by Nickel Nanotube Array as Supercapacitor Electrode with Improved Rate Capability" (2016). *Graduate Theses and Dissertations*. 15978.
<https://lib.dr.iastate.edu/etd/15978>

This Thesis is brought to you for free and open access by the Iowa State University Capstones, Theses and Dissertations at Iowa State University Digital Repository. It has been accepted for inclusion in Graduate Theses and Dissertations by an authorized administrator of Iowa State University Digital Repository. For more information, please contact digirep@iastate.edu.

**Carbon nanotube thin film supported by nickel nanotube array as supercapacitor
electrode with improved rate capability**

by

Hosein Monshat

A thesis submitted to the graduate faculty
in partial fulfillment of the requirements for the degree of

MASTER OF SCIENCE

Major: Mechanical Engineering

Program of Study Committee:

Shan Hu, Major Professor

Reza Montazami

Robbyn Anand

Jaime J. Juarez

Chao Hu

Iowa State University

Ames, Iowa

2016

Copyright © Hosein Monshat, 2016. All rights reserved.

DEDICATION

Every challenging work needs self-efforts as well as guidance of elders especially those who were very close to our heart. My humble effort I dedicate to my sweet and loving

Father, Mother & Dr. Shan Hu,

whose affection, love and encouragement make me able to get such success and honor.

TABLE OF CONTENTS

	Page
LIST OF FIGURES	v
LIST OF TABLES	viii
NOMENCLATURE	ix
ACKNOWLEDGMENTS	x
ABSTRACT	xi
CHAPTER I: INTRODUCTION.....	1
1. Supercapacitance Mechanism.....	1
1.1. Electrostatic double-layer	1
1.2. Pseudocapacitance	2
2. Supercapacitors' characterization techniques	3
2.1. Cyclic voltammetry	3
2.2. Electrochemical impedance spectroscopy	6
2.3. Frequency analysis	12
2.4. Cyclic charge and discharge	13
2.5. Leakage current	15
3. Carbon Nanotubes.....	15
4. Current Collectors Advantages	17
5. Electrophoretic Deposition	18
CHAPTER II: EXPERIMENTAL AND SIMULATION	21
CHAPTER III: RESULTS	24
1. Constant-Current EPD vs. Constant-Voltage EPD: Experiment and Simulation.....	24
2. Constant-Current EPD With Different EPD Current and Time.....	27

3. Cyclic Voltammetry (CV) and Rate Capability.....	31
3.1. Ni-foil/f-CNT.....	31
3.2. Ni-foam/f-CNT.....	32
3.3. NiNT/f-CNT.....	33
4. Electrochemical Impedance Spectroscopy	36
4.1. Leakage current resistance.....	36
4.2. Relaxation time.....	37
5. Leakage Current Test.....	38
6. Galvanostat Charge-Discharge, Energy and Power Density, and Cyclic Stability.....	39
7. Combined Thermal Analysis and Fourier Transform Infrared Spectroscopy (FT-IR)	40
CHAPTER IV: SUMMARY AND CONCLUSIONS.....	43
REFERENCES	45

LIST OF FIGURES

	Page
Figure 1. Electric double layer capacitors charge storage mechanism [2].....	2
Figure 2. Reversible mechanisms of pseudocapacitance, A) Underpotential deposition, B) Redox pseudocapacitance C), Intercalation pseudocapacitance [4].....	3
Figure 3. Cyclic voltammetry, capacitor voltage and current sweeping vs. time.	4
Figure 4. CV plot for a non-ideal supercapacitor.....	6
Figure 5. Sinusoidal Current Response in a Linear System.....	7
Figure 6. Nyquist plot.	8
Figure 7. Bode plot of a supercapacitor.	9
Figure 8. Impedances in A) Series, B) Parallel.....	10
Figure 9. A) Cyclic charge and discharge test and B) <i>IR</i> drop for a non-ideal supercapacitor.	14
Figure 10. Single-wall and Multi-wall Carbon nanotubes structure.....	16
Figure 11. Conductive current collectors A) 2D and B) 3D.	18
Figure 12. Electrophoretic deposition of functionalized CNTs [57].	19
Figure 13. Multiphysics models of the electrophoretic deposition of functionalized CNTs to nickel nanotube current collector.	23
Figure 14. EPD of f-CNT onto nickel substrate via A) Constant voltage EPD and B) Constant current EPD.	24

Figure 15. Multiphysics simulation of electrical field and f-CNT particle distribution around nanotubes in constant voltage – EPD.	25
Figure 16. Multiphysics simulation of the electrical field and f-CNT particle distribution around nanotubes in constant current – EPD.	26
Figure 17. Electrical field distribution around individual NiNTs and B) SEM image of NiNT/f-CNT showing faster deposition of f-CNT on tips of NiNTs.	27
Figure 18. Microstructure of f-CNTs coated on, A) Nickel nanotubes/1500x, B) Nickel-foam/1500x, C and D) Nickel-foil/1500x and 30000x.	28
Figure 19. SEM image showing f-CNT on A) NFL1040_5000x, B) NFL1040_30000x, C) NFM1540_500x and D) NFM1540_30000x.	29
Figure 20. SEM images of f-CNT on NiNTs for Set A, B and C.	30
Figure 21. SEM image showing f-CNT “umbrella” on NiNT array in NNT1540 and NNT1520.	31
Figure 22. Rate capability of Ni-foam/f-CNT Electrodes produced with different EPD conditions.	32
Figure 23. Rate capability of Ni-foam/f-CNT Electrodes produced with different EPD conditions.	33
Figure 24. Rate capability of Ni-foil/f-CNT Electrodes produced with different EPD conditions.	34
Figure 25. A) CV curve of NFL1040, NFM1540 and NNT1510 and B) Rate capability of NFL1040 (83 F/g at 1 mV/sec), NFM1540 (183 F/g at 1 mV/sec) and NNT1510 (200 F/g at 1 mV/sec).	35
Figure 26. Nyquist plot for NFL1040, NFM1540 and NNT1510.	36

Figure 27. Imaginary capacitance versus frequency for NFL1040, NFM1540 and NNT1510.	38
Figure 28. Leakage current test results for NNT1510, NFM1540 and NFL1040.	39
Figure 29. A) CCD curves of NNT1510 at different current densities, B) Four cycles of CCD for NNT1510 at 2.5mA, C) Ragone plot of sample NNT1510 and D) Cyclic stability of NNT1510 at scanning rate of 50 mV/Sec.	40
Figure 30. Combined thermogravimetric analysis and FT-IR Spectroscopy of NNT1510.	41
Figure 31. IR gas analysis of NNT1510.	42

LIST OF TABLES

	Page
Table 1. Common Electrical Elements.....	9
Table 2. EPD parameters for constant current - EPD	22
Table 3. Calculated parameters based on Randles circuit.....	37

NOMENCLATURE

CCD	Cyclic Charge and Discharge
CNT	Carbon Nano-tube
CV	Cyclic Voltammetry
ECD	Electrochemical Deposition
EDLC	Electric Double layer Capacitors
EIS	Electrochemical Impedance Spectroscopy
EPD	Electrophoretic Deposition
ESR	Equivalent Series Resistance
f-CNT	Functionalized Carbon Nano-tube
FT-IR	Fourier Transform Infrared Spectroscopy
FTO	Fluorine Doped Tin Oxide
MWCNT	Multi-Walled Carbon Nano-tube
NFL	Nickel Foil
NFM	Nickel Foam
NiNT/NNT	Nickel Nano-tube
PPY	Polypyrrole
rGO	Reduced Graphene Oxide
SEM	Scanning Electron Microscopy
SWCNT	Single-Walled Carbon Nano-tube
TGA	Thermogravimetric Analysis
UGF	Ultrathin Graphite

ACKNOWLEDGMENTS

I would like to thank my committee chair, *Dr. Shan Hu*, and my committee members, *Dr. Reza Montazami*, *Dr. Robbyn Anand*, *Dr. Jaime J. Juarez*, and *Dr. Chao Hu*, for their guidance and support throughout the course of this research.

In addition, I would also like to thank my friends, colleagues, the department faculty and staff for making my time at Iowa State University a wonderful experience. I want to also offer my appreciation to those who were willing to participate in my surveys and observations, without whom, this thesis would not have been possible.

ABSTRACT

Functionalized carbon nanotube (f-CNT) thin films were deposited onto plain nickel foil, nickel foam and nickel nanotube (NiNT) arrays using electrophoretic deposition (EPD) to fabricate a CNT-based supercapacitor. A two-dimensional multiphysics model of the EPD process was established to investigate f-CNT particles deposition on nickel substrates with constant voltage and constant current modes. Combined scanning electron microscopy and electrochemical analysis elucidate that the best rate capability is achieved when f-CNT thin films conformally wrap NiNTs and provide the fastest electron transport between active materials and current collectors. The effect of micro and nanostructured current collectors on the rate capability of CNT-nickel supercapacitors was studied by deposition of f-CNT on nickel foil, nickel foam as well as nickel nanotubes (NiNT). 51% capacity retention was calculated for NiNT/f-CNT when scanning rate was increased from 1 to 50 mV/sec in cyclic voltammetry test whereas, nickel foam/f-CNT and nickel foil/f-CNT kept 35% and 30% of their initial capacities in the same test. The specific capacitance of 200 F/g and capacitance retention of 90% after 1000 cycles was obtained for NiNT/f-CNT cell. Frequency analysis demonstrates a higher ability of NiNT/f-CNT to get polarized with the lowest dielectric relaxation time as small as 0.044 sec.

Keywords: Functionalized carbon nanotube, Nickel nanotube arrays, Nanostructured current collector, Multiphysics model, Electrophoretic deposition, Electrochemical deposition, Supercapacitor, Dielectric relaxation time.

CHAPTER I: INTRODUCTION

Like batteries, supercapacitors are energy storage devices. Stored energy in batteries is produced by chemical reactions however supercapacitors store energy by physical separation of electrical charges [1]. Supercapacitors can provide high levels of electrical power and offer long operating lifetimes. They can deliver more energy per unit mass (energy density) than electrolytic capacitors and also higher charge-discharge rate than batteries [1, 2]. Furthermore, supercapacitors enjoy longer cycle-life, experience no memory effect and are safer compared with batteries [1].

1. Supercapacitance Mechanism

Electrostatic double-layer and pseudocapacitance are the two primary distinguished mechanisms for charge storage in supercapacitors [1].

1.1. Electrostatic double-layer

In electric double layer capacitors (EDLC), electrical energy is electrostatically stored by separation of charges between the conductive electrode and the electrolyte (Fig.1) [2]. Separation charge distance in a double layer is on the order of angstroms. The double layer comprises the excess charge stored on the electrode surface and the charge stored in the Stern, Helmholtz, and diffuse layers. The Helmholtz double layer model is a simplified description of the true double layer structure. [1, 3]. This double layer is formed as ions from the solution adsorb onto the electrode surface. EDLCs are not limited to charge transfer kinetics. Therefore,

they can be charged or discharged much faster than commercial batteries, which means they have higher energy releasing rate (power density) than rechargeable batteries [1, 3]. In the Macroscopic level, the capacitance of an EDLC is given by following equation [3]:

$$C = \varepsilon_r \varepsilon_0 A / d \quad (1)$$

where ε_r is the dielectric constant dielectric which is related to the materials properties, ε_0 is permittivity of free space, A is the surface area of active material which is in contact with the electrolyte, and d is the double layer thickness.

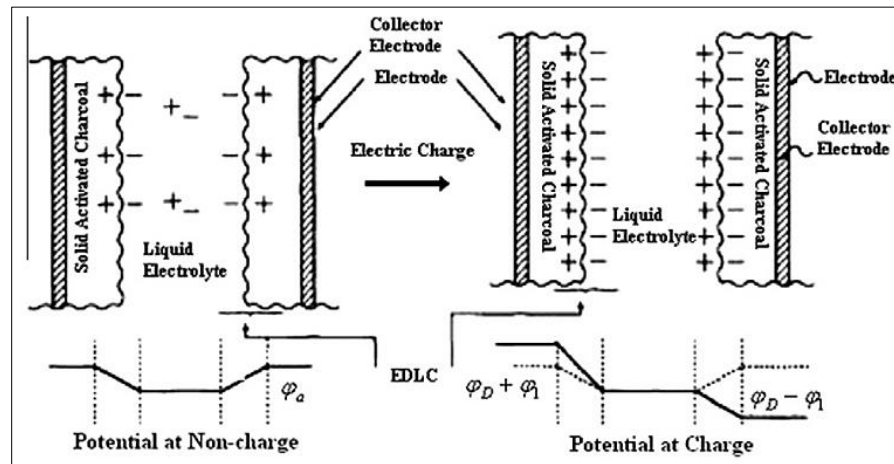


Figure 1. Electric double layer capacitors charge storage mechanism [2].

1.2. Pseudocapacitance

Electron charge-transfer between electrolyte and electrode could occur due to the fast sequence of reversible faradaic redox or intercalation process, that phenomena are the basis of pseudocapacitance behavior (Fig.2) [4].

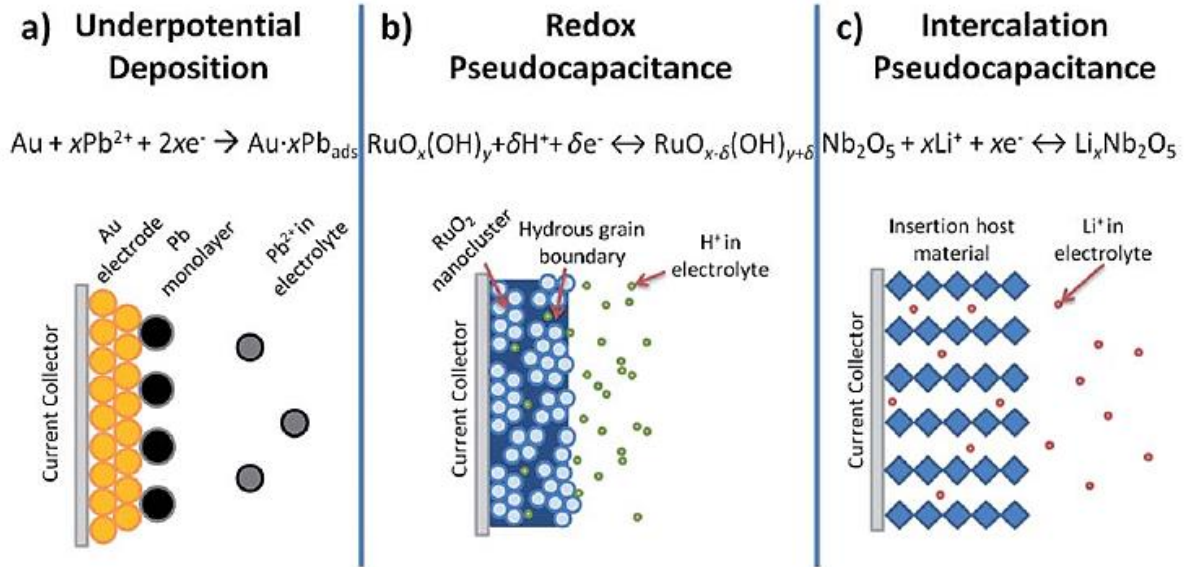


Figure 2. Reversible mechanisms of pseudocapacitance, A) Underpotential deposition, B) Redox pseudocapacitance C), Intercalation pseudocapacitance [4].

Pseudocapacitors that could undergo higher reversible surface redox reactions rate can store more charges per volume than regular double-layer capacitors [5]. Higher surface redox reactions rate increases both energy density of lithium-ion batteries as well as power density of supercapacitors [5].

2. Supercapacitors' characterization techniques

There are different well-known tests to evaluate electrochemical properties of a supercapacitor such as cyclic voltammetry, electrochemical impedance spectroscopy, cyclic charge, and discharge as well as leakage current test, which are briefly explained in following sections.

2.1. Cyclic voltammetry

Cyclic voltammetry (CV) plots electrochemical cell current variation while a linear voltage-ramp is swept over a voltage range as shown in Fig.3. Usually, voltage sweep is

repeated between two limit potentials during the CV test, each pair of opposite direction sweeps is called a cycle [6, 7].

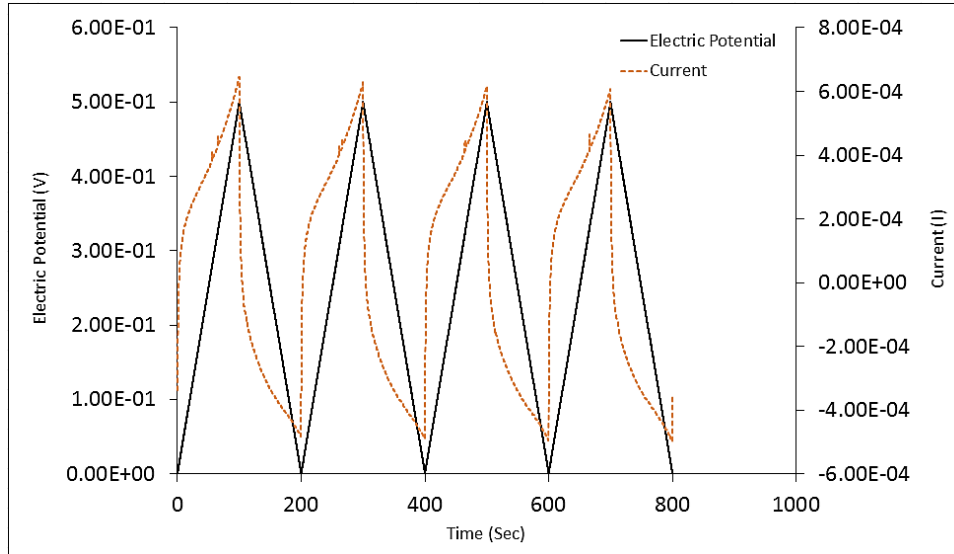


Figure 3. Cyclic voltammetry, capacitor voltage and current sweeping vs. time.

CV test could be done using two or three electrodes in the cell, employing three electrode setup makes it possible to study the one electrode while it is not going to be affected by the electrochemistry of other electrodes [8]. The three electrodes are:

- Working Electrode: the electrode which is being tested.
- Reference Electrode: The electrode which has a constant electrochemical potential.
- Counter Electrode: An electrode which completes the circuit and is an inert electrode.

In two-electrode setup, the reference and counter electrodes should be connected to one side of the capacitor. The potential difference between the working and the reference electrode will be measured and recorded. Usually, a voltage scan rate between 0.1 mV/s to 1 V/s is used for CV test of a supercapacitor [7, 9]. Lower voltage scanning rate allows the side reactions tracking in CV plot. However, the test may take several hours to be done. Ideally, capacitors

should have the same charge storage capacity at different charge/discharge rates however in reality, due to the mass and charge transport limitations; they demonstrate lower capacitance at higher charge/discharge rates. Using a range of different scanning rates make it possible to calculate the rate capability which can present the capacitor's ability to retain its high specific capacitance (capacitance per mass of active material) at high charge/discharge rate. The rate capability can be calculated by dividing the capacitance obtained in the fastest scanning rate to the one obtained by the slowest scanning rate [8]. The working principle of capacitors dictates that more electron transport paths and faster mass transport of solution phase ions (for pseudocapacitors, electron transport between electrode and electrolyte) increase cell rate capability [6, 7, 8].

For an ideal supercapacitor, the CV plot would be a rectangle however for a non-ideal supercapacitor, equivalent series resistance (ESR) causes the slow rise in the current and rounds two corners of the rectangle (Fig.4) [6, 7]. Due to the electrical resistance in the electrode, contacts, and the electrolyte, real commercial supercapacitors suffer power-loss during charge and discharge. The sum of the electrical resistances that mentioned above is called equivalent series resistance.

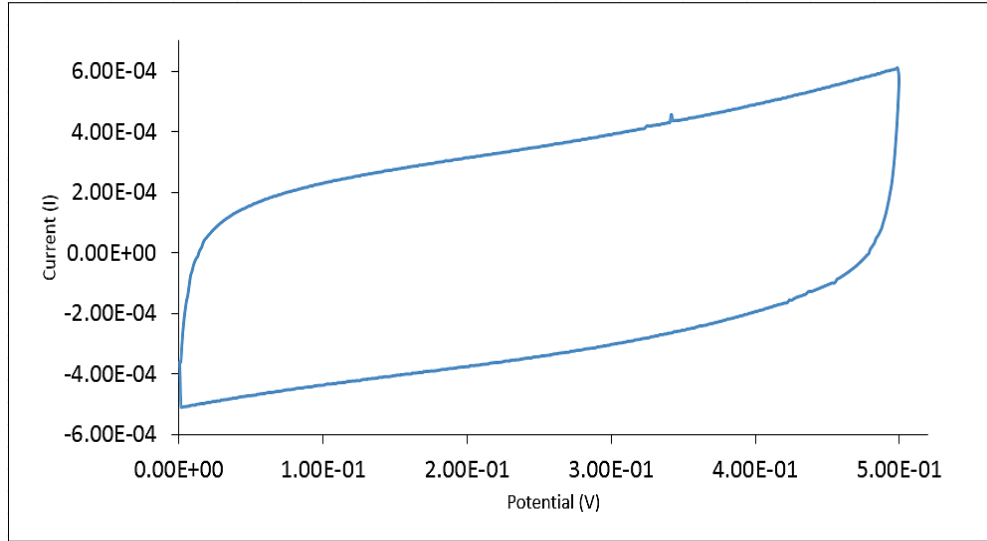


Figure 4. CV plot for a non-ideal supercapacitor.

2.2. Electrochemical impedance spectroscopy

Electrochemical impedance spectroscopy (EIS) is a standard method to measure the capacitance and the ESR of a non-ideal supercapacitor. Applying a small AC potential to an electrochemical cell and measuring cell current is the basis of electrochemical impedance spectroscopy [10]. Having different electrical elements in a circuit makes it difficult to use simple ohmic resistance, in these situations using the concept of impedance is highly preferred. Impedance shows the ability of the circuit to resist the flow of electrical current [11].

Usually, 1 to 10 mV AC signal is applied to the cell during EIS test, which is small enough to hold the system in linear/pseudo-linear condition [10]. For a linear system, current respond to an applied sinusoidal potential would be a sinusoid at the same frequency but shifted in phase (Fig.5).

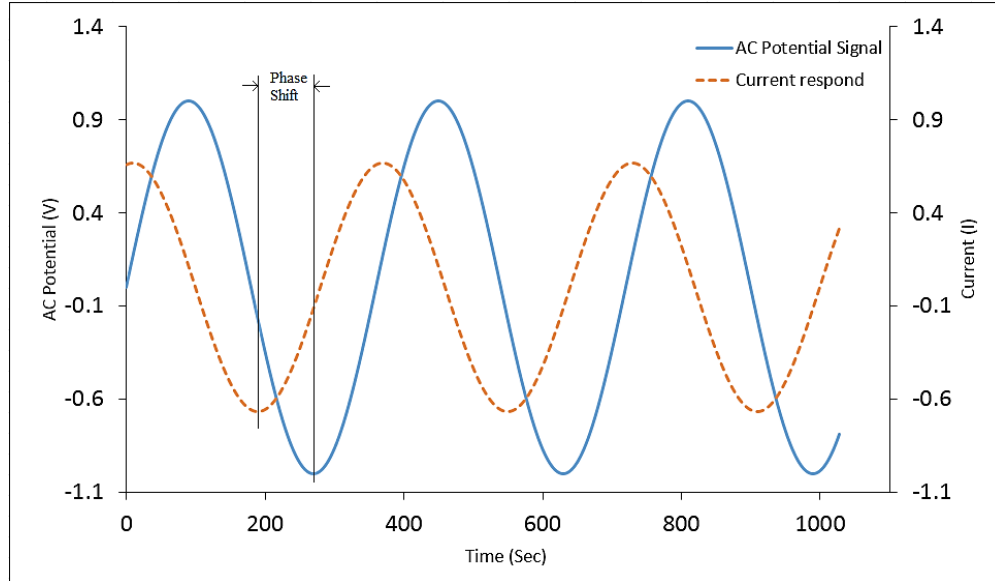


Figure 5. Sinusoidal Current Response in a Linear System.

Applying a sinusoidal potential as a function of time with the radial frequency ω and the amplitude E_0 , has the form:

$$E = E_0 \sin(\omega t) \quad (2)$$

For a linear electrical system the current response has the form:

$$I = I_0 \sin(\omega t + \phi) \quad (3)$$

where I_0 is the max current amplitude and ϕ is the phase shift. The impedance of the system is calculated as [10]:

$$Z(\omega) = \frac{E(\omega)}{I(\omega)} = \frac{E_0 \sin(\omega t)}{I_0 \sin(\omega t + \phi)} = Z_0 \frac{\sin(\omega t)}{\sin(\omega t + \phi)} \quad (4)$$

where Z_0 is the impedance magnitude. Using Euler relationship (Eq.5) the impedance could be represented as complex number as defined in Eq.6 [10]:

$$\exp(j\phi) = \cos(\phi) + j\sin(\phi) \quad (5)$$

$$Z(\omega) = \frac{E(\omega)}{I(\omega)} = Z_0(\cos\phi + j\sin\phi) \quad (6)$$

Using Eq.6 and plot the real part on X-axis and imaginary part on Y-axis, we get a "Nyquist Plot" as shown in Fig.6. In Nyquist plot, each point represents the impedance at one frequency. A vector from the origin to each point of a Nyquist plot has a length of $|Z|$ and make an angle with X-axis which called "phase angle" [11].

The main shortcoming of Nyquist plot is that it is not possible to tell the frequency related to the each point by taking a look at data points. To overcome that disadvantage of Nyquist plot, we can use "Bode Plot" in which both $|Z|$ and the phase angle are plotted on the y-axis versus log frequency on the x-axis (Fig.7) [12].

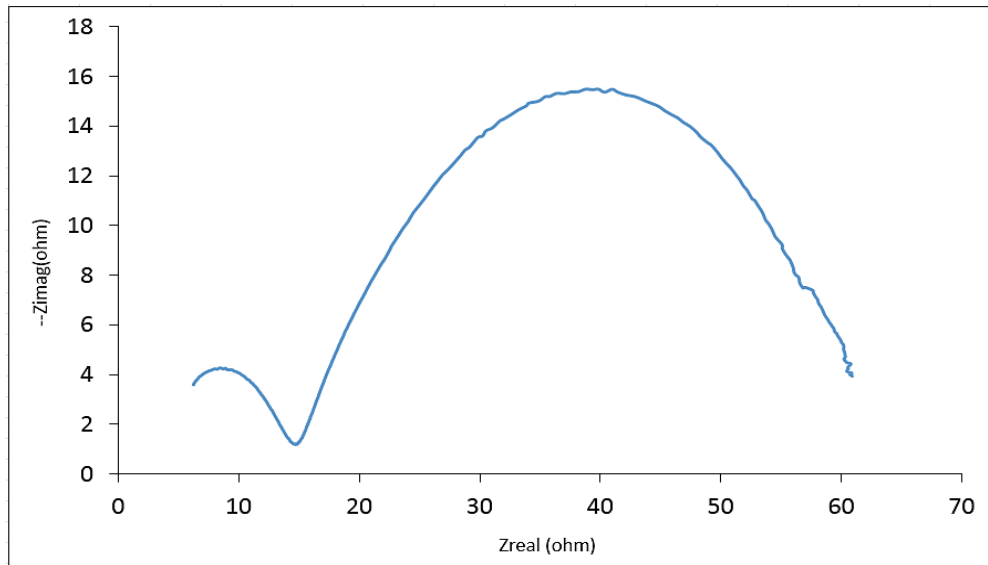


Figure 6. Nyquist plot.

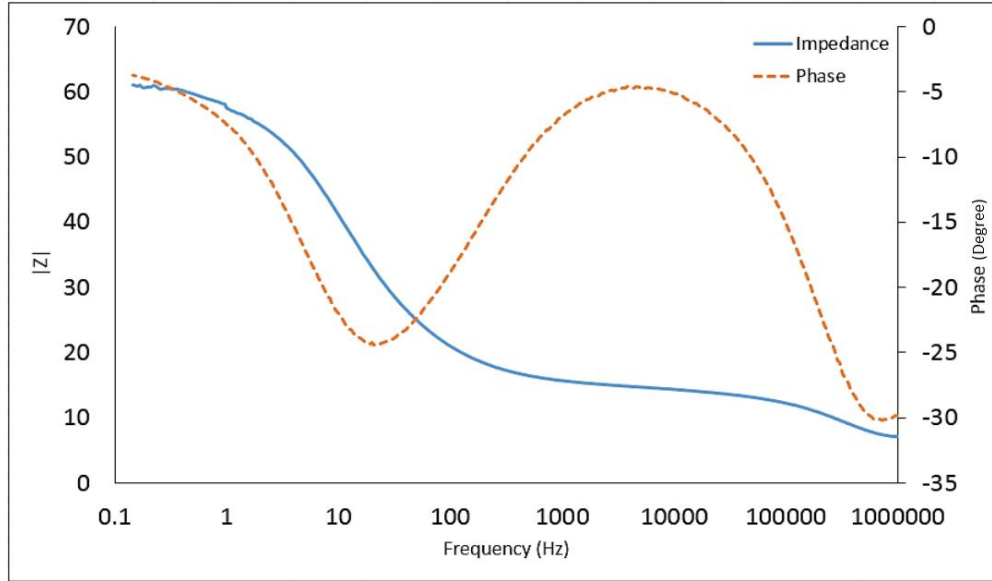


Figure 7. Bode plot of a supercapacitor.

For carrying out an electrochemical analysis of EIS data, an equivalent electrical circuit model (include common electrical elements such as resistors, inductors as well as capacitors) is employed to fit a mathematical model on discrete EIS data. The electrical equivalent circuit should be designed based on the physical electrochemistry of the system [12]. Voltage-current relationship and the impedance of some common electrical elements are listed in Table 1[12].

Table 1. Common Electrical Elements

Element	Current Vs. Voltage	Impedance
Resistor	$V = IR$	$Z = R$
Capacitor	$I = C \frac{dV}{dt}$	$Z = \frac{1}{j\omega C}$
Inductor	$V = L \frac{dI}{dt}$	$Z = j\omega L$

Arranging basic elements in parallel and series pattern and designing a multi-elements circuit, as shown in Fig.8, makes it possible to model an electrochemical cell [12].

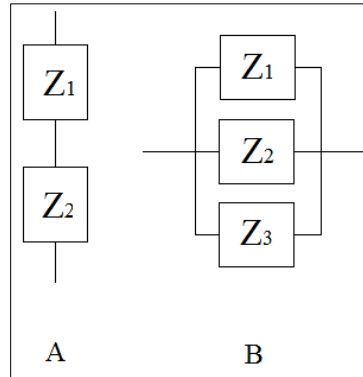


Figure 8. Impedances in A) Series, B) Parallel.

There are simple formulas to calculate the linear impedance of circuit elements in both parallel and series combination, as follows [12]:

$$\left\{ \begin{array}{l} \text{Equivalent impedance in series:} \\ \text{Equivalent impedance in parallel:} \end{array} \right. \quad \begin{array}{l} Z_{eq} = \sum_{i=1}^N Z_i \\ Z_{eq} = \frac{1}{\sum_{i=1}^N \frac{1}{Z_i}} \end{array} \quad (7)$$

For series resistor combination, both resistance and impedance go up. However, series capacitors increase the equivalent impedance while decrease the capacitance [10, 12]. As mentioned before, understanding the physical phenomenon such as electrolyte resistance, polarization resistance, charge transfer resistance, diffusion, and coating capacitance of the electrochemical cell is required to design an electrical equivalent circuit for EIS data analysis.

2.2.1. Electrolyte resistance

Ionic solution resistance is an important parameter for the impedance analysis of an electrochemical cell, which depends on different parameters such as temperature, ionic

concentration as well as ions type [11, 13]. Electrolyte electrical resistance could be calculated using Eq.8:

$$R_E = \frac{1}{k} \frac{L}{A} \quad (8)$$

where k is the electrical conductivity of the solution ($1/\Omega$), A is the area of a bounded electrolyte with the length of L .

2.2.2. Polarization resistance

Polarization occurs when an overpotential is applied at the electrode-electrolyte interface without resulting in electron transfer. For example, a system that approaches the behavior of an ideally polarizable electrode would be an Au electrode with an alkane thiol monolayer coating at the surface. The monolayer prevents faradaic reactions (passivates the electrode) over a wide potential range. In contrast, an example of a non-polarizable electrode is a reference electrode (e.g., Ag/AgCl) for which an incrementally applied potential leads to a large increase in faradaic current. Reference electrodes are not easily polarized (moved away from their equilibrium potential). Polarization resistance is measured as the slope of the current-potential curve at low overpotential, and it is the same as charge transfer resistance. [13].

2.2.3. Charge transfer resistance

If the reaction which occurs on the surface of the electrode is a single, kinetically-controlled electrochemical reaction, then the resistance that prevents the current from flowing through such a reaction is called charge transfer resistance. Charge transfer resistance depends on different parameters such as temperature, electrolyte ion concentration as well as potential [13].

2.2.4. Diffusion

The impedance that created by diffusion is called Warburg impedance which depends on the potential perturbation frequency [10, 14]. Warburg impedance is larger at low frequencies since diffusing reactants have to diffuse farther. In Bode plot, the Warburg diffusion leads to 45° shift of the phase plot, and in a Nyquist plot that will show up as a straight line with the slope of 45° at lower frequencies [10, 13, 14].

2.2.5. Constant phase element

Non-ideal capacitors (commercial double-layer capacitors) act like a constant phase which is a capacitor with an impedance as defined below [10]:

$$Z_{CPE} = \frac{1}{(j\omega)^{\alpha}Y_0} \quad (9)$$

where Y_0 is the capacitance and α is an exponent that is equal to 1 for an ideal capacitor, and less than 1 for a constant phase element.

2.3. Frequency analysis

To study dielectric relaxation time of supercapacitors (response of a dielectric medium to an external, oscillating electric field), \check{C} -frequency plot should be generated, where \check{C} is imaginary part of capacitance and can be calculated as follows [15]:

$$Z(\omega) = Z_{real}(\omega) + j Z_{imaginary}(\omega) \quad (10)$$

$$\check{C}(\omega) = \frac{Z_{real}(\omega)}{\omega|Z(\omega)|^2} \quad (11)$$

where $Z(\omega)$ is the impedance of the electrochemical system and ω is pulsation. Real and imaginary values of impedance are x and y axis of Nyquist plot, respectively. The relaxation time constant correspond to a transition of the resistive behavior of the supercapacitor to

capacitive behavior is calculated by $1/f_0$, where f_0 is pick-frequency of \dot{C} - frequency plot.

Relaxation time constant could also be presented by following equation [16]:

$$\tau_0 = R \times C_0 \quad (12)$$

where R is ESR and C_0 is specific capacitance considering the mass of active materials. Large relaxation time means that the charges which are electro-absorbed onto the electrode surface cannot be completely extracted from the electrode during discharge. There is irreversible charge-discharge happening when the charge/discharge frequency (as determined by the scan rate and the upper charge limit) is higher than the relaxation frequency (f_0) of the electrode. As a result, it is expected to see a better rate capability for the sample which has lower relaxation time.

2.4. Cyclic charge and discharge

Cyclic Charge-Discharge (CCD) is a common test to investigate the performance and cycle-life of supercapacitors and batteries, which usually done at a constant current. Each loop of charging and discharging is called a cycle (Fig.9.A). Usually, repetitive cycles of CCD follows capacitance drop, the number of cycles indicates the cycle-life of the capacitor (cyclic stability), which is in the order of hundreds of thousands of cycles for commercial capacitors [17, 18].

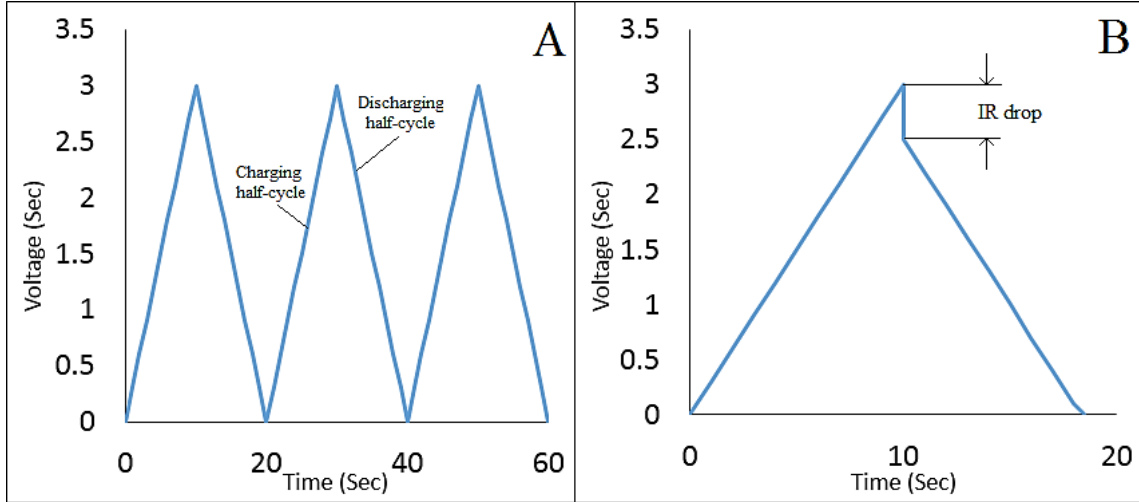


Figure 9. A) Cyclic charge and discharge test and B) IR drop for a non-ideal supercapacitor.

For an ideal capacitor, the slope of the CCD curve is constant and is defined by:

$$\frac{dV}{dt} = \frac{I}{C} \quad (13)$$

where I is the constant current of CCD test and C is the cell capacitance.

The shape of CCD curve can change to an exponential form by increasing the capacitor self-discharge. Moreover, a large voltage drop at each half-cycle occurs if the cell has a large ESR, which significantly reduces power density and capacitance of the cell (Fig.9.B) [17, 18]. The energy and power density are two important characteristics of each supercapacitor, which indicate how much energy can be released by a cell and how fast it can be achieved, and are defined by Eq.14 and Eq.15 [17]:

$$E = CV^2/2 \quad (14)$$

$$P_{max} = V^2/(4 \times m \times R_{drop}) \quad (15)$$

$$R_{drop} = V_{drop}/I \quad (16)$$

where C is specific capacitance (F/g) obtained by discharging curve at different currents, V is the voltage of discharging, R_{drop} is equivalent series resistance calculated from IR drop and m is the mass of active material. Plotting power density versus energy density (called Ragone plot) can give a performance comparison of different supercapacitors [17, 18].

2.5. Leakage current

A non-ideal charged capacitor cannot hold its constant voltage unless it is supplied by a constant current called leakage current that can be modeled as a resistance in parallel with the capacitor [19]. Current leakage results in self-discharging of a supercapacitor and reflects the flow of current when the cell is charged. Hence, lower leakage current will promote the supercapacitors performance. Leakage current can be measured in at least two ways [19, 20]:

- Measure the required current to maintain a specific voltage limit while a DC voltage is applied to the capacitor.
- Put a charged capacitor in open circuit condition and measure the voltage change during self-discharge.

3. Carbon Nanotubes

Carbon nanotubes (CNTs) have been studied recently as a novel electronic and electrochemical material. Carbon nanotubes are divided into single (SWCNT) and multi-walled carbon nanotubes (MWCNT), based on the rolling graphite sheet structure, as shown in Fig.10 [21]. SWCNT structure is like wrapping a one-atom-thick layer of graphite called graphene into a seamless cylinder with the average diameter of 0.75-3 nm and the average length of 1-50 μm [22]. SWCNTs Behave as a semiconductor can easily be modified to tailor

properties as an “ink” have high heat conductivity and the yield strength higher than carbon steels [23].

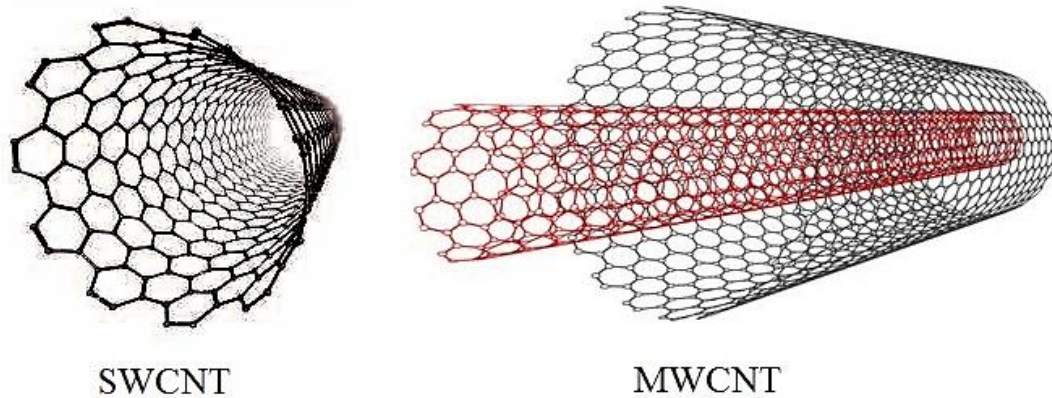


Figure 10. Single-wall and Multi-wall Carbon nanotubes structure.

MWCNTs could be considered as more than two concentric rolled-graphene layers which have an approximate distance of 100 nm and the average diameter of 2-30 nm [22]. CNTs can show outstanding application as both electrodes and transducer components in biosensors [24]. Aligned MWNT grown on the platinum substrate could be used for the development of an amperometric biosensor. The opening and functionalization by oxidation of the nanotube array allow for the efficient immobilization of the model enzyme, glucose oxidase [24].

Due to the low electrical resistivity, high electrolyte accessibility, high charge transport capability, and high specific surface area of CNTs, they could be considered as attractive electrode materials for high-performance supercapacitors [25, 26]. Functionalized CNT [27-30], carbon composite of CNT [31, 32, 33], and nanocomposite of CNT with electrochemically active materials [34-47] have been proposed as supercapacitor electrode materials.

Peng *et al.* used chemical oxidation method to polymerize polypyrrole (PPy) onto reduced graphene oxide/carbon nanotube (rGO/CNT) which shows specific energy and power density of 14 Wh kg^{-1} and 6.62 kWkg^{-1} [48]. He *et al.* fabricated nitrogen-doped carbon nanotubes (N-CNT)/carbon foam (CF) employing chemical vapor deposition method, as a flexible supercapacitor [49]. N-CNTs/CF cell exhibited a power density of 69.3 kW kg^{-1} and the capacitance retention of above 95% after 5000 cycles at 50 A g^{-1} [49]. Yi *et al.* developed a supercapacitor CNT/nickel oxide nanosheets core-shell, porous carbon polyhedrons (PCPs) and aqueous KOH solution as a positive electrode, negative electrode, and electrolyte, respectively [33]. CNT/NiO/PCP cell shows a high specific capacitance of 996 (F/g) at 1 A g^{-1} , exhibits maximum energy density of 25.4 Wh kg^{-1} at a power density of 400 W kg^{-1} and the capacitance retention of 93% after 10,000 cycles [50]. In the case of graphene composite electrodes, amidation reaction was used to synthesize a graphene–CNT composite with lamellar structure [51]. By making complementary bonding between the graphene oxide and CNTs prevent the agglomeration of CNTs [51].

4. Current Collectors Advantages

It has been well established in battery and supercapacitor research that the use of current collectors and highly conductive active materials will lower the overall resistance of the electrode and improve electron transport (Fig.11). Micro-device components assembly on a conductive 3D framework is state of the art approach for fabricating micro-devices with three-dimensional architecture [52]. Using 3D porous current collectors reduces the total weight of the cell, allows a large mass of active materials to be deposited and makes strong current collector-active material binding [53].

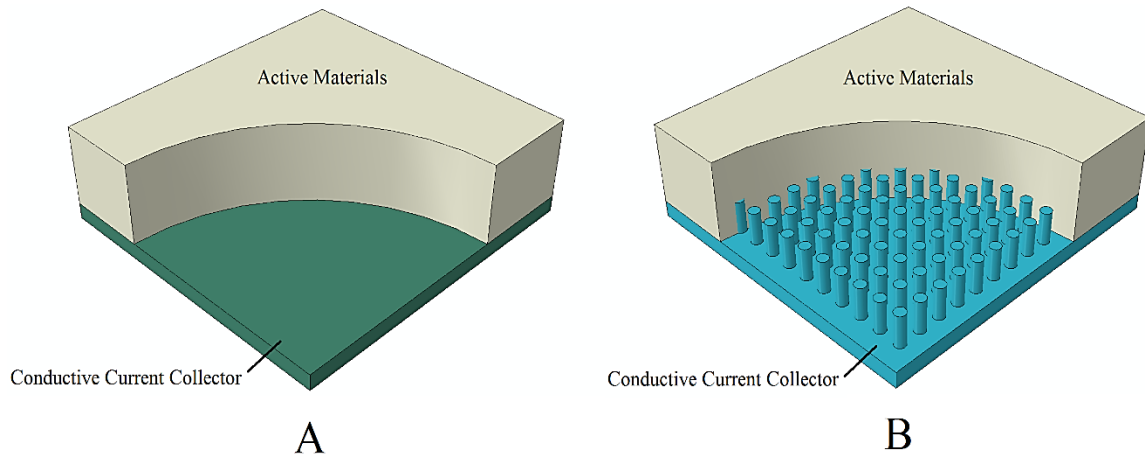


Figure 11. Conductive current collectors A) 2D and B) 3D.

Implementing conductive 3D current collectors (e.g. metal foams and nanostructures) provide advantages of low internal resistance rather than flat ones and accelerate electron transport [53, 54]. As an example, ultra-thin graphite thin film (UGF) acts as a highly conductive 3D framework network facilitates electron transport during charge and discharge of Ni(OH)₂/UGF cell and [55]. 3D nanostructures afford increased interfacial area between electrode and electrolyte and ultimately improved rate capability of the CNT/nickel nanotube (NiNT) supercapacitor, provided that CNTs conformally coated on NiNTs.

5. Electrophoretic Deposition

Electrophoretic deposition (EPD) can provide a conformal layer of active materials on the surface of an electrically conductive 3D current collector [53]. In this method, two conductive substrates are immersed with in an electrolyte; then an electric field is applies between the two electrodes to attract charged particles dispersed in the electrolyte towards a designated electrode (Fig.12). It worth to note that EPD can be carried out with constant current or constant voltage modes. Accumulation of charged particles, which are attracted towards electrode with opposite polarization, will result in the formation of a solid layer of dispersed

particles on the electrode surface. EPD has advantages of being scalable, low-cost, and solution-processed. Compared with other solution-based deposition methods, such as drop-casting, EPD provides higher controllability and is a promising technique to produce uniform and homogeneous microstructures [56]. Electrolyte conductivity is the main challenge of implementing EPD as an electrode fabrication method.

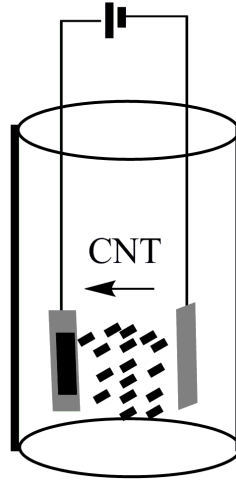


Figure 12. Electrophoretic deposition of functionalized CNTs [57].

Pristine CNT is neutrally charged and non-polarized but functionalized CNTs (f-CNT) have functional groups such as carboxylate group which provides negatively charged particles of carbon nanotubes that can be uniformly dispersed in water. f-CNT can be uniformly dispersed into water to enable solution-based manufacturing of CNT electrodes such as EPD [58]. Appropriate functional groups can even introduce pseudocapacitance behavior and improve the overall charge storage capacity of CNT electrodes [59].

While most of existing studies on CNT-based supercapacitors have been focused on achieving high specific capacitance (F/g or F/cm^3) and impressive specific capacitance values have been reported, only limited work has been done to increase the rate capability of CNT-based supercapacitors. Current study aims to develop a CNT-based electrode with high specific

capacitance and rate capability. Using advantages of CNT, current collector, and nanostructured structures, a rational design of electrode is developed in the current study to achieve high capacity and rate capability.

In current research, EPD is used to conformally coat f-CNT thin films onto nickel foil with a smooth surface (Ni-foil), nickel foam with micro-size pores (Ni-foam) as well as NiNT arrays with nano-sized surface roughness. CNTs are functionalized with carboxylic groups, which develop weak negative charge in water. Under an applied electric field, f-CNT particles holding negative charges are bonded with the conductive substrate by moving towards the positive electrode [58, 60, 61]. A uniform layer of f-CNT will be formed via f-CNT particles accumulating on the conductive substrate. The rate performances of the resulting three sets of electrodes are compared, and the structure-performance relationship is identified. Moreover, a 2D simulation has been done to study the difference between constant current and constant voltage EPD. Related experiments and simulation steps are explained in the next chapter.

CHAPTER II: EXPERIMENTAL AND SIMULATION

In the current research, f-CNT was made by refluxing 0.1 g of pristine multiwalled CNTs in concentrated nitric acid and sulfuric acid (1:3 v/v) for 20 minutes at 110 °C. Corning filter with 0.22 μ m pore size was used to wash away acids and collect f-CNTs. f-CNTs were dried at 40 °C on a hot plate overnight and weighed. 0.05 mg/ml f-CNT solutions was made by dispersing f-CNTs into deionized water with bath sonication (Branson 2510) for 1 hour.

Electrochemical deposition (ECD) was used to grow nickel nanotube (NiNT) current collector. Specifically, Watt's nickel electroplating solution with 75 wt% of nickel sulfide, 15 wt% of nickel chloride and 10 wt% of boric acid in 200 ml of DI water was used as an electrolyte for ECD and Ni-foil was used as sacrificing electrode. Isopore track-etched polycarbonate template (Sigma Aldrich) with 13 mm diameter and 400 nm pore size was used as templates for nanotube growth. A gold seed layer was sputtered onto one side of the template followed by subsequent growth of a thin nickel film by ECD for 1 minute at 20 (V). Then the other side of the template was exposed to the nickel plating solution, and NiNTs were grown inside the pores of the template by ECD for 6 min at 1.5 volts. Finally, the filter was removed by chloroform to yield freestanding nickel nanotubes.

Nickel foils, nickel foams and nickel nanotubes were coated with f-CNTs by employing EPD for the time window between 5 to 15 seconds, current of 10 to 40 (mA) (Table 2) and using 0.05 mg/ml f-CNT solutions. Samples were divided into three sets based on the EPD

current value (Set A 5mA, Set B 10mA, and Set C 15 mA). For each EPD current, three different EPD times (10, 20 and 40 sec) were used.

Table 2. EPD parameters for constant current EPD

Current Collectors				EPD Current (mA)	EPD time (min)
Sets	Ni-foil substrate	Ni-foam substrate	NiNT substrate		
Set A	NFL510	NFM510	NNT510	5	0:10
	NFL520	NFM520	NNT520	5	0:20
	NFL540	NFM540	NNT540	5	0:40
Set B	NFL1010	NFM1010	NNT1010	10	0:10
	NFL1020	NFM1020	NNT1020	10	0:20
	NFL1040	NFM1040	NNT1040	10	0:40
Set C	NFL1510	NFM1510	NNT1510	15	0:10
	NFL1520	NFM1520	NNT1520	15	0:20
	NFL1540	NFM1540	NNT1540	15	0:40

Since f-CNTs have weak negative charge, a positive polarization was applied to the nickel electrode and a negative polarization to the FTO glass as the counter electrode. The distance between the two electrodes was kept at 1.5 cm. The mass loading of f-CNT was determined by weighing the sample before and after f-CNT deposition with an analytical scale with 0.001mg readability. Also, thermogravimetric (TGA) analysis was performed on the f-CNT/NiNT electrode to confirm the mass loading of f-CNT. TGA was done in N₂/O₂ atmosphere between 40 to 1000 °C with Netzsch STA449 F1 thermal analyzer. After EPD, the electrode was dried on the hot plate at 50 °C for 6 hours.

The microstructures of the electrodes were investigated by high resolution scanning electron microscopy (SEM; FEI Quanta 250). A two-electrode symmetric supercapacitor was fabricated with 1 M LiCl as the electrolyte for electrochemical measurements. Cyclic voltammetry (CV), electrochemical impedance spectroscopy (EIS), leakage current and galvanostatic charge/discharge tests were done with Gamry Reference 3000 potentiostats/galvanostat for electrochemical characterization of the samples.

To investigate the difference between the electrical fields made by constant current and constant voltage EPD, a 2D Multiphysics model was employed using COMSOL 4.5 as shown in Fig.13. Moreover, particle tracking of functionalized CNT particles was done using combined Electric Currents and Charged Particle Tracing physics models in COMSOL.

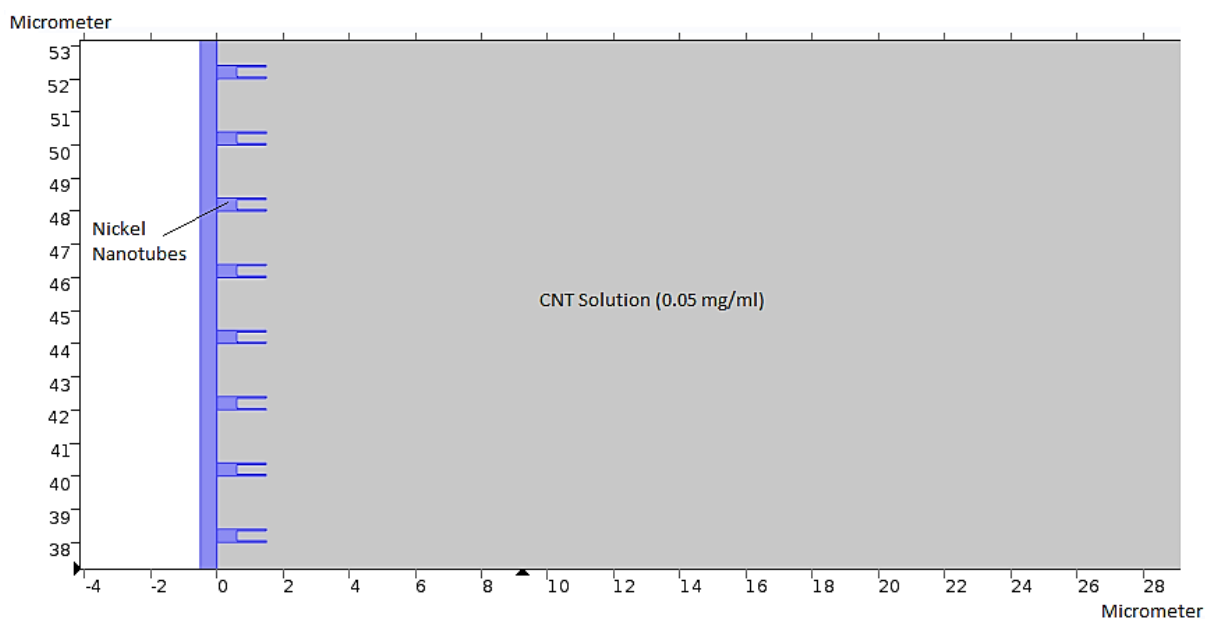


Figure 13. Multiphysics models of the electrophoretic deposition of functionalized CNTs to nickel nanotube current collector.

CHAPTER III: RESULTS

1. Constant-Current EPD vs. Constant-Voltage EPD: Experiment and Simulation

Fig.14 shows f-CNT deposition on NiNTs with constant-current EPD (10 mA for 40 seconds) and constant-voltage EPD (10 V for 40 seconds). It is clearly shown that constant-current EPD produced an overall uniform coating of f-CNT on the NiNTs. However, the constant-voltage EPD deposit a thick layer of f-CNT on NiNTs at the edge of the sample but sparse f-CNT coverage in central regions.

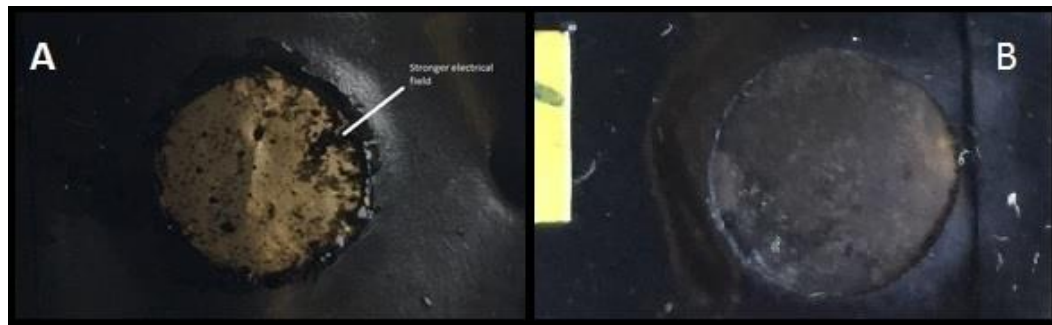


Figure 14. EPD of f-CNT onto nickel substrate via A) Constant voltage EPD and B) Constant current EPD.

To elucidate the reason for the observed difference in these two approaches, 2D Multiphysics models of the EPD processes were established via COMSOL 4.5. Multiphysics simulation results reveal that non-uniform distribution of electric field over the NiNT in constant voltage EPD is the main reason for the non-uniform f-CNT deposition. As can be seen in Fig.15, the electrical field at the edge of NiNT is much stronger than that in the center area,

and the f-CNT particle density around the edge of the sample is much higher than that in their central region, which agrees with experimental results.

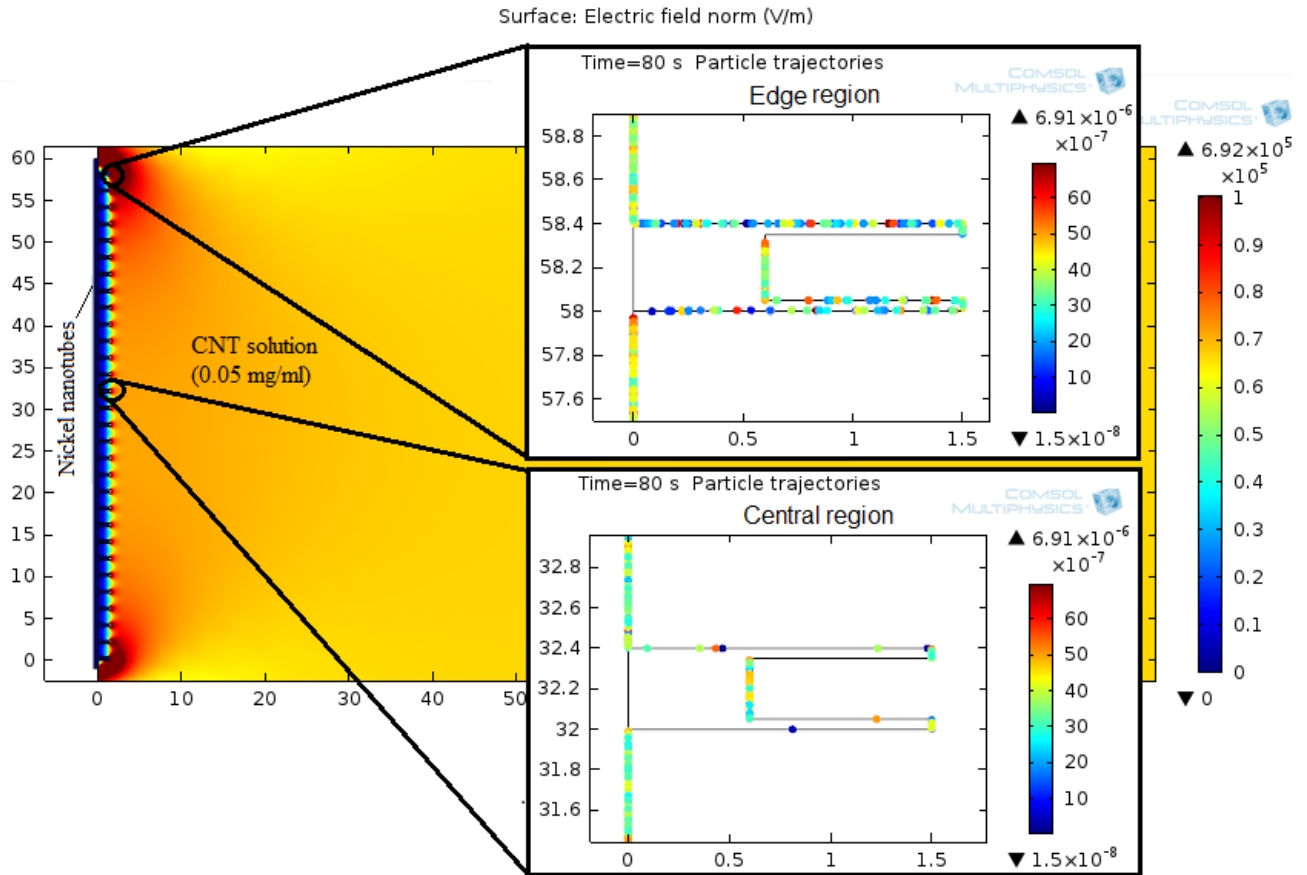


Figure 15. Multiphysics simulation of electrical field and f-CNT particle distribution around nanotubes in constant voltage – EPD.

On the other hand, electrical field distribution is smooth and uniform for constant-current EPD and the densities of charged particle (i.e. f-CNTs) at the edge and the central region are almost the same, as demonstrated in Fig.16.

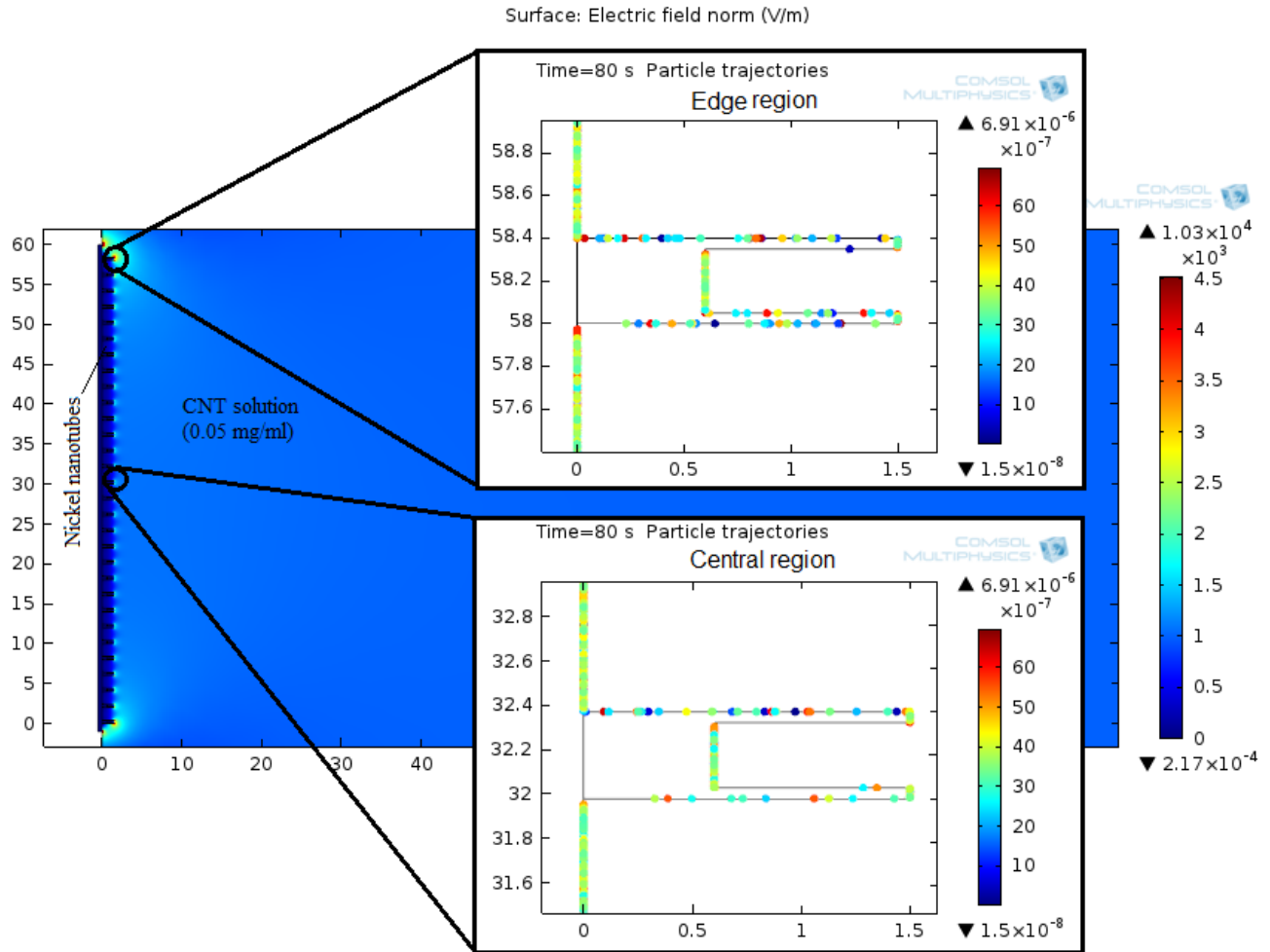


Figure 16. Multiphysics simulation of the electrical field and f-CNT particle distribution around nanotubes in constant current – EPD.

Electrical field distribution along individual NiNT was also investigated with the Multiphysics model. Electrical field strength drops by moving from the tip of NiNT to the root (Fig.17.A). Hence, it is expected to see more f-CNTs attracted to the tip of the nanotubes, which is in good agreement with SEM image of NiNT/f-CNT sample (Fig.17.B). Keeping the above results in mind, using shorter NiNTs is recommended for developing a uniform coating of f-CNTs on individual NiNT. However, reducing the aspect ratio of the NiNT will also reduce interfacial area between NiNT and f-CNT and slower the charge transport. In this research, it is found that NiNT grown by 6-min of ECD provides satisfactory performance.

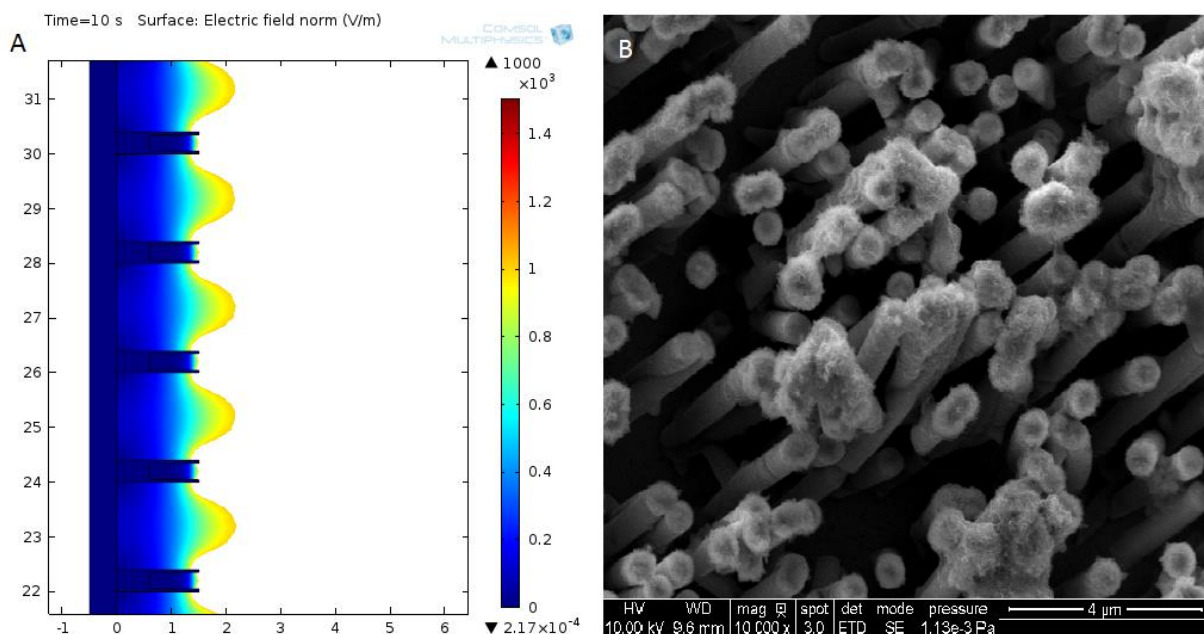


Figure 17. Electrical field distribution around individual NiNTs and B) SEM image of NiNT/f-CNT showing faster deposition of f-CNT on tips of NiNTs.

2. Constant-Current EPD With Different EPD Current and Time

Fig.18 illustrates microstructure of the samples made by EPD, as can be seen, constant-current EPD produced overall uniform coating of f-CNT on the NiNTs (Fig.18.A). Using a broad range of EPD current and time make f-CNT deposition rate controllable, so that, f-CNTs can cover the surface of Ni-foam without blocking pores (Fig.18.B). Moreover, f-CNTs could be uniformly deposited onto the smooth surface of nickel foil using constant-current EPD (Fig.18.C and Fig18.D).

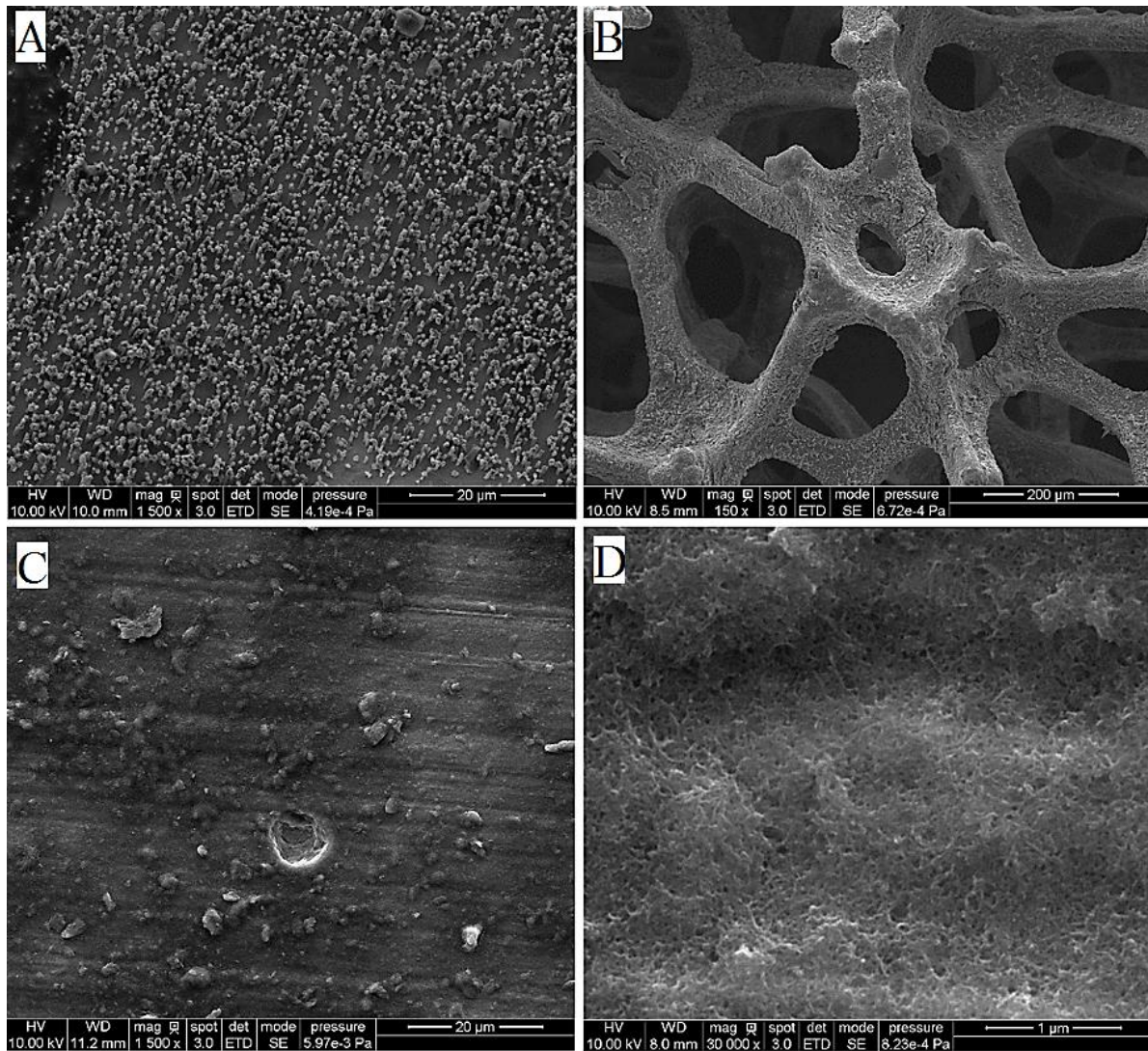


Figure 18. Microstructure of f-CNTs coated on, A) Nickel nanotubes/1500x, B) Nickel-foam/1500x, C and D) Nickel-foil/1500x and 30000x.

Fig.19.A and B illustrate f-CNTs coating on a nickel plate, NFL1040, a uniform layer of functionalized carbon nanotubes is formed on the nickel substrate, using constant current EPD. By receding current collector surface, electrical field strength decreases due to the internal electrical resistance of the f-CNT layer. As a result, a thick layer of f-CNT reduces the ability to attract and hold electrical charges, rate capability, and current leakage resistivity. Therefore, it is strongly preferred to make a thin layer of f-CNT on the nickel to keep both

capacitance and rate capability. Fig.19.C and D show microstructure of Ni-foam/f-CNT electrode, NFM1540, a uniform f-CNT coating layer is formed on the nickel foam matrix but did not block the pores. Using Ni-foam will provide more surface area of active materials. Hence, it is expected to see a higher rate capability than Ni-foil/f-CNT electrode.

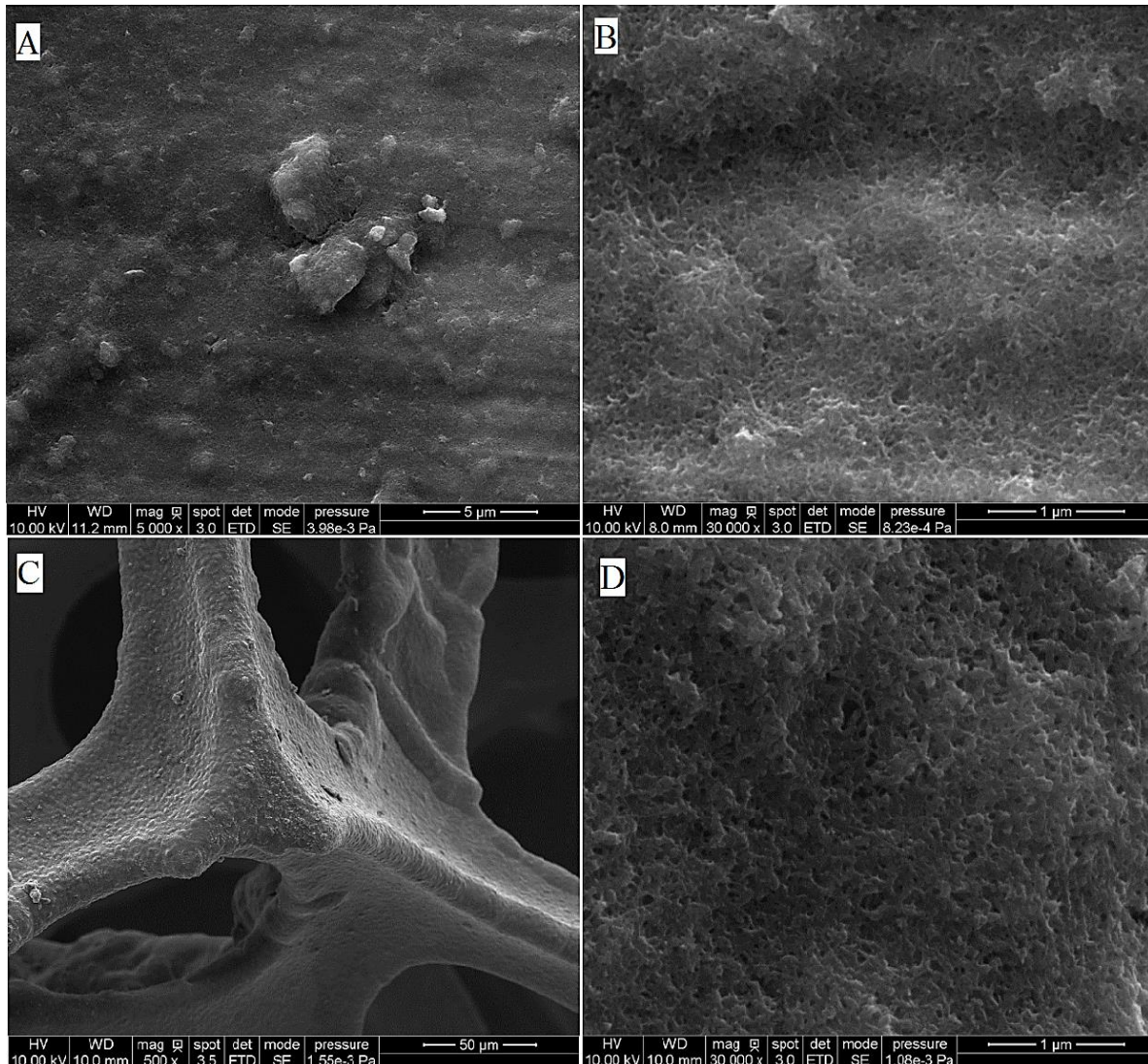


Figure 19. SEM image showing f-CNT on A) NFL1040_5000x, B) NFL1040_30000x, C) NFM1540_500x and D) NFM1540_30000x.

Fig.20 shows the SEM images of NiNT/f-CNT electrodes in all Sets. By increasing EPD time, highly conductive f-CNT bridges formed between nanotubes, which introduce more

electron transport paths, hence, better rate capability behavior is expected. The morphology of NiNT/f-CNT electrodes of Set B are similar to those in Set A. However; Set C is showing obviously different morphology from that of other samples. In addition to f-CNT bridges that are found in all other samples, SEM of NNT1540 shows large-area and continuous f-CNT thin film covering the nanotubes like an “umbrella” (Fig. 21).

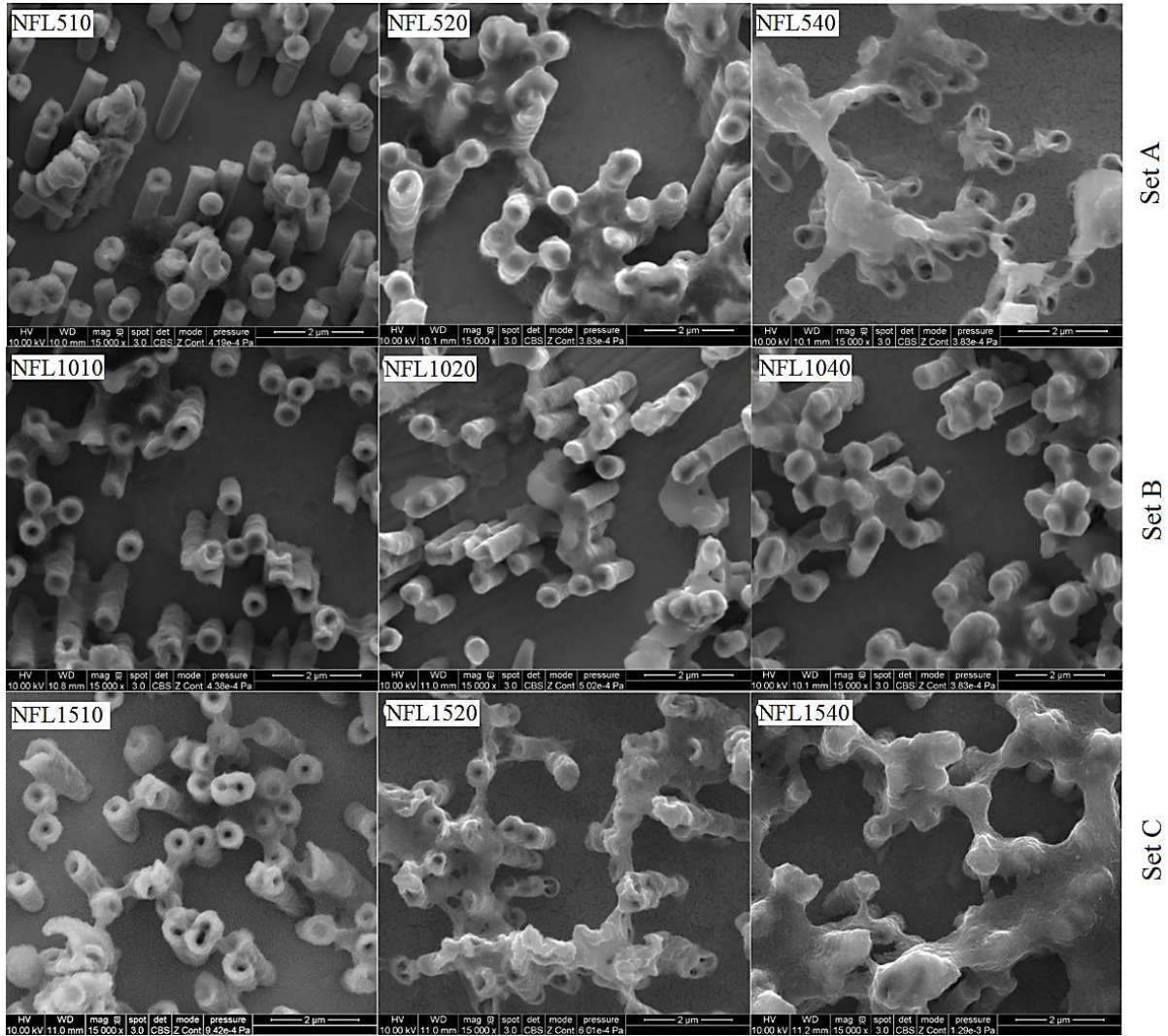


Figure 20. SEM images of f-CNT on NiNTs for Set A, B and C.

In fact, the f-CNT “umbrella” started to appear in NNT1520 as isolated islands, and as the EPD time increases, these isolated islands develop into continuous thin film over a large

area in NNT1540. Combining the Multiphysics simulation results, it is proposed that the formation of the f-CNT umbrella is caused by the stronger electric field on the tip of the nanotube, which causes f-CNT particles to accumulate faster at the tip. The f-CNT particles first form a “canopy” on top of an individual nanotube. After prolonged EPD time, individual canopies are bridged together by newly deposited f-CNT particles to form a continuous thin film covering multiple NiNTs like an umbrella. It is expected that this large-area “umbrella” structure has a negative effect on the rate capability because it prevents the ions in electrolyte from accessing the electrode area located underneath the umbrella.

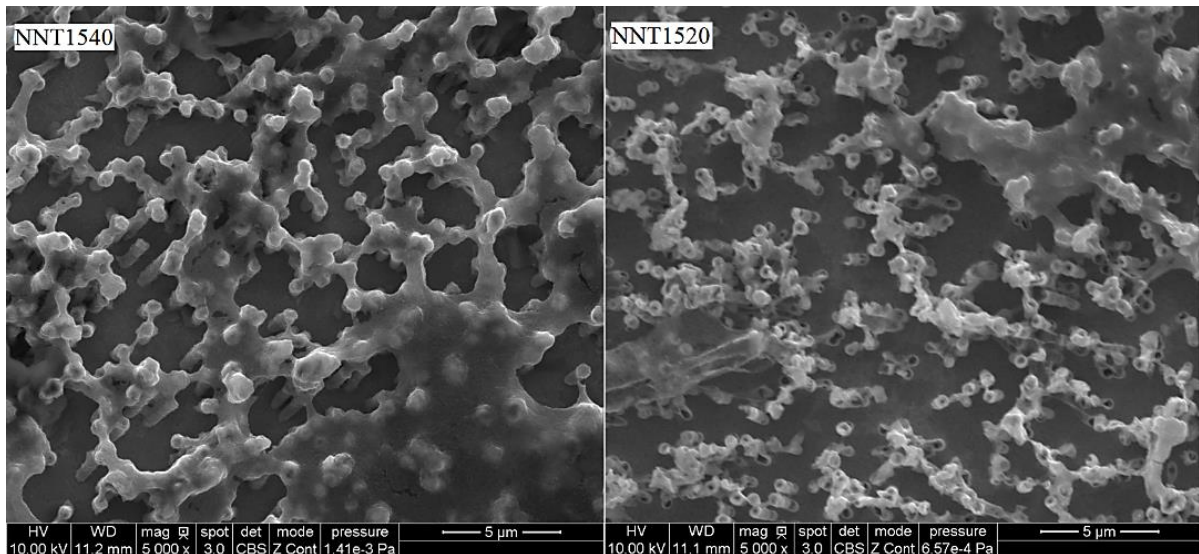


Figure 21. SEM image showing f-CNT “umbrella” on NiNT array in NNT1540 and NNT1520.

3. Cyclic Voltammetry (CV) and Rate Capability

3.1. Ni-foil/f-CNT

Rate capability of Ni-foil/f-CNT cells was calculated based on CV test for scanning rates of 1 to 50 mV/sec (Fig.22). In the best case, rate capability of 30% was obtained for NFL1040, however, for the NFL/f-CNT cells of set B and set C, the rate capability remains

almost 29%. During deposition of f-CNT on nickel foil, a thick layer of active material rapidly forms on the surface of the current collector. By receding current collector surface, the internal resistance of f-CNT attenuates electrical field strength around the surface of active material. Hence, forming a thick layer of f-CNTs on the nickel substrate can decrease the ability to hold electrical charges. As a result, after formation of a thin f-CNT layer on the nickel foil, increasing the EPD time and current decreases electron transfer rate and attenuates the electrical field around the f-CNT layer, which causes lower rate capability.

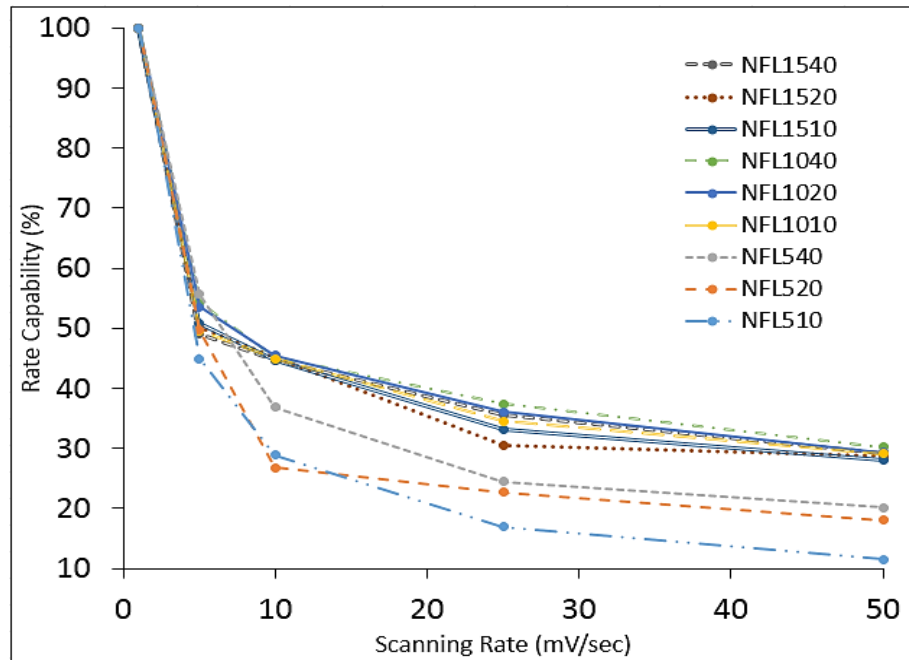


Figure 22. Rate capability of Ni-foam/f-CNT Electrodes produced with different EPD conditions.

3.2. Ni-foam/f-CNT

Rate capability of Ni-foam/f-CNT is shown in Fig.23, as can be seen, increasing EPD time and current gradually increases rate capability, since, more active materials are bind to the nickel current collector by increasing EPD time and current. NFM1540 shows the highest rate capability of 35% among all Ni-foam/f-CNT cells. Considering the higher surface area of

Ni-foam than Ni-foil, it needs stronger electrical field (EPD current) or longer deposition time to form a layer of f-CNTs as thick as Ni-foil/f-CNT electrode and rate capability plot may reach a plateau for longer f-CNT deposition time or higher EPD current which used in current study. Higher rate capability of Ni-foam/f-CNT than Ni-foil/f-CNT cells can be due to the higher effective mass loading of active material, higher ability to release stored electrical charges during discharging and higher leakage current resistance.

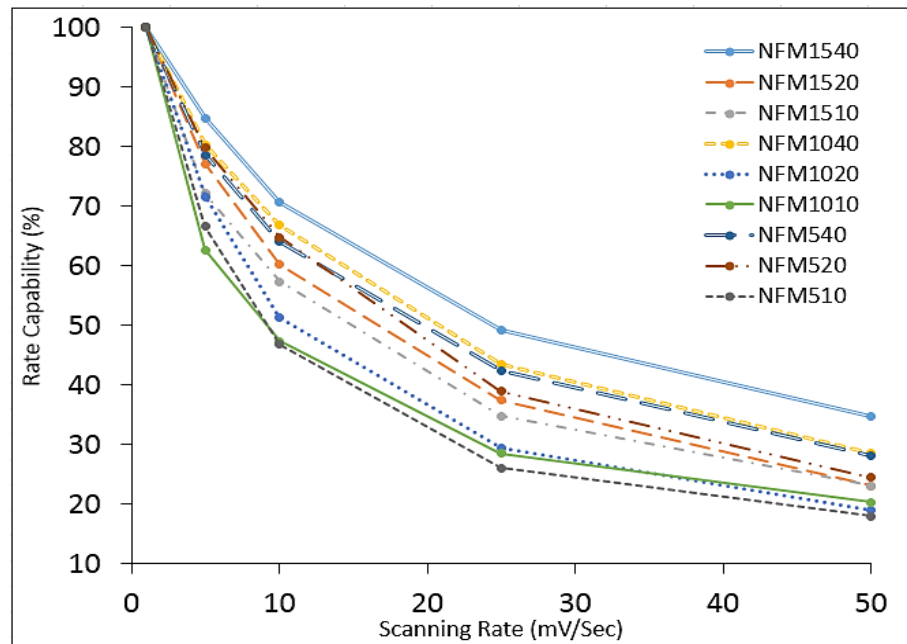


Figure 23. Rate capability of Ni-foam/f-CNT Electrodes produced with different EPD conditions.

3.3. NiNT/f-CNT

Fig.24 exhibits rate capability is overall increasing with higher EPD current for NiNT/f-CNT cells. The effect of EPD current on rate capability is more significant with lower EPD times: rate capability increases by 28.3% after increasing EPD current from 5 to 15 mA in 10-second EPD, whereas, it increases by 7.3% in same current range with 40 sec of deposition time. As can be seen, Set C (highest EPD current among three sets) shows the higher rate

capability. Increasing EPD current results in higher amount of f-CNT particles attracted towards the metal substrate for a fixed time window. Subsequently, there will be more f-CNT bridges formed between NiNTs, resulting in faster electron transport and better rate capability. NNT1510 shows the highest rate capability among all three samples in set C, which is 51% when scanning rate increases from 1 to 50 mV/sec, it has the lowest EPD time, however. Lower rate capability of NNT1520 and NNT1540 is due to the formation of “umbrella structure” by f-CNTs at prolonged EPD time, which prevents the electrolyte to meet the current collector located beneath of umbrella layer (Fig.21).

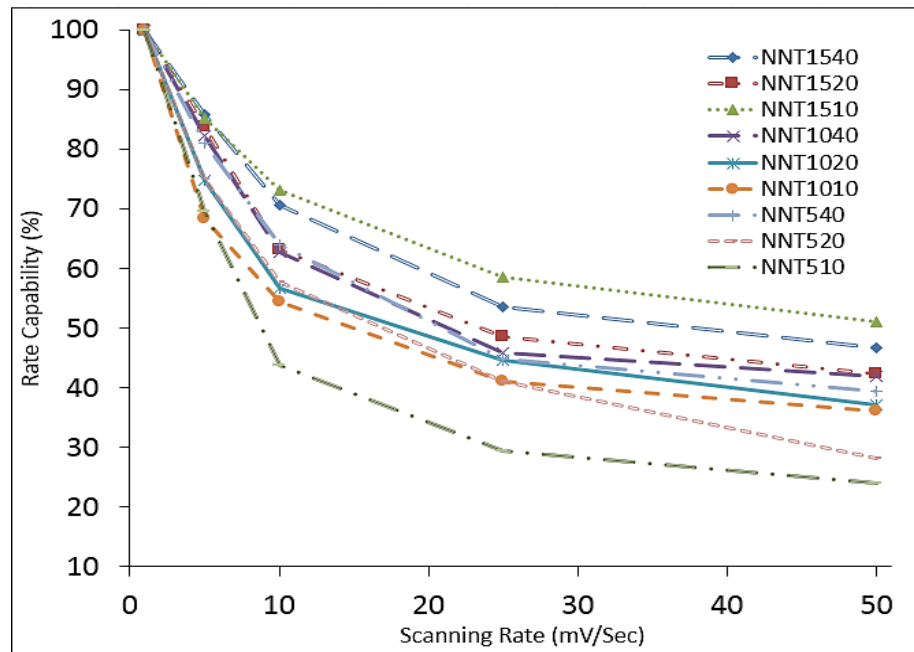


Figure 24. Rate capability of Ni-foil/f-CNT Electrodes produced with different EPD conditions.

In summary, high EPD current and long EPD time increase the mass loading of f-CNT which has a positive effect on the rate capability of Ni-foil/f-CNT and NiNT/f-CNT cells initially. However, due to the anisotropic deposition rate, excessive f-CNT will eventually

cover the top of NiNTs and block mass transport pathway between the electrolyte and the roots of NiNTs, hence, decrease rate capability. In Ni-foil/f-CNT cell, excessive f-CNT could attenuate the electrical field around f-CNT layer and decrease both specific capacitance and rate capability due to increasing current leakage. Fig.25.A shows CV curve for NFL1040, NFM1540, and NNT1510, at the scanning rate of 50 mV/sec.

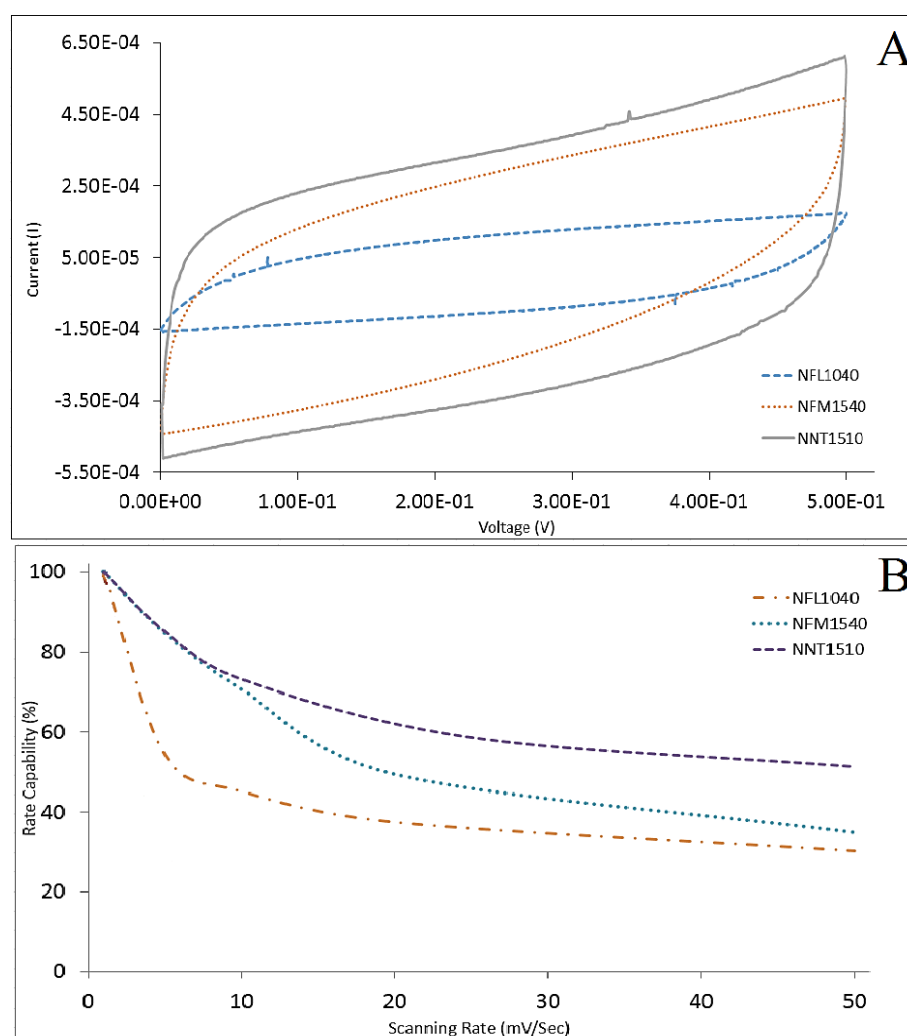


Figure 25. A) CV curve of NFL1040, NFM1540 and NNT1510 and B) Rate capability of NFL1040 (83 F/g at 1 mV/sec), NFM1540 (183 F/g at 1 mV/sec) and NNT1510 (200 F/g at 1 mV/sec).

For a supercapacitor with small equivalent series resistance (ESR), CV plot would be rectangular with straight sides. Hence, NNT1510 behaves more like an ideal supercapacitor

considering the shape of CV curve. Since the same type of active material is used to build all f-CNT-based electrodes for the current study, rate capability difference between three sets of electrodes should be addressed to the structure of current collectors in each category. 3D structures such as NiNT arrays make higher surface area and more efficient contact between nickel substrate and CNT particles, which lower leakage current and increase the rate capability (Fig.25.B). EIS test was employed to investigate frequency behavior and leakage current resistance of the samples.

4. Electrochemical Impedance Spectroscopy

4.1. Leakage current resistance

Electrochemical impedance spectroscopy was done for the frequency range of 1 Hz to 1MHz and AC/DC voltage of 1 mV and 1 V respectively. EIS results of samples with the best rate capability in each set of nickel current collector/f-CNT cells (NNT1510, NFM1540, and NFL1040) are shown in Fig.26.

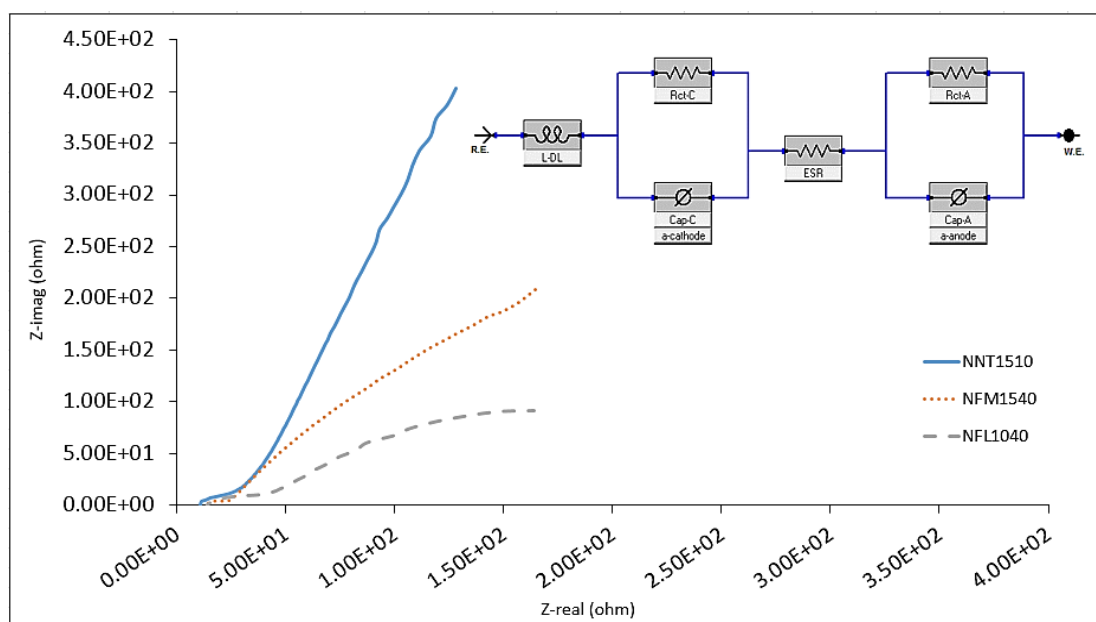


Figure 26. Nyquist plot for NFL1040, NFM1540 and NNT1510.

An equivalent circuit was used to model EIS discrete data for all of the samples (Fig.26), considering the physical meaning of the elements used in the circuit, Rct shows the leakage current resistance in each case. Table 3 shows Rct value of NNT1510, NFM1540, and NFL1040, NNT1510 demonstrate higher Rct (5730 Ω) than NFM1540 (1340 Ω) and NFL1040 (322 Ω). Therefore, the leakage current of NiNT/f-CNT cell is lower than Ni-foam/f-CNT which also has a lower leakage current than Ni-foil/f-CNT. Furthermore, NNT1510 Nyquist plot is closer to an ideal supercapacitor, having a straight line inclined to y-axis at the low-frequency region, which represents faster ion diffusion in the structure of NNT1510 [58] (Fig.26).

Table 3. Calculated parameters based on Randles circuit.

Parameters	NFL1040	NFM1540	NNT1510
Rct-cathode (Ω)	27.97	9.43	19.75
Rct-anode (Ω)	322.31	1340.12	5730.27
Goodness of Fit	0.00012	0.00006	0.00005

4.2. Relaxation time

The frequency behavior of NFL1040, NFM1540 and NNT1510 was investigated using complex capacitance. As can be seen in Fig.27, NNT1510 demonstrates the lowest relaxation time and it has the highest rate capability among other cells, which previously confirms by CV test in section 3. EIS result confirms that using 3D structures in current collector made more electrons transport paths, leads to lower electron transport resistance and relaxation time. Hence, higher rate capability can be achieved. To quantify the leakage current of NNT1510, NFM1540, and NFL1040, leakage current test has been done.

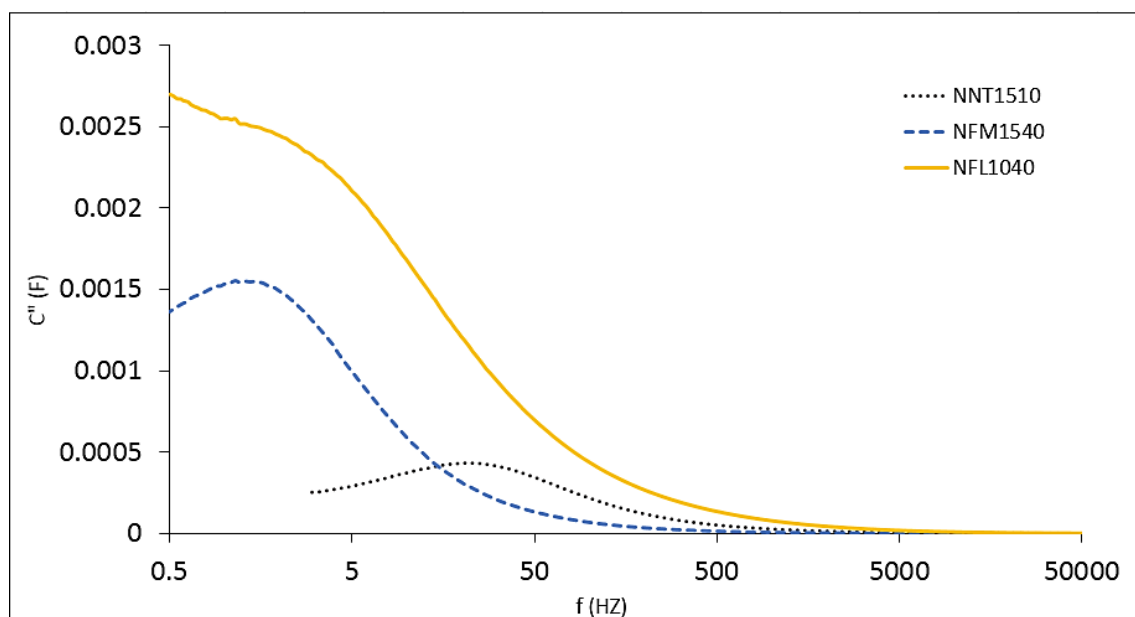


Figure 27. Imaginary capacitance versus frequency for NFL1040, NFM1540 and NNT1510.

5. Leakage Current Test

A DC potential of 0.5 V applied to the selected samples under test, and currents variation were measured to study leakage current in each case. Fig.28 shows current drop versus time for NNT1510, NFM1540, and NFL1040. As can be seen, the leakage current of NiNT/f-CNT cell ($3.8 \mu\text{A}$) is lower than Ni-foam/f-CNT ($4.79 \mu\text{A}$) and Ni-foil/f-CNT ($34.67 \mu\text{A}$). These results confirm that using 3D current collector decreases electron transport resistance, hence, increase the supercapacitor performance and efficiency. These results also double confirm R_{ct} variation trend which obtained by EIS results in 4.1. Charge-discharge behavior, energy density, power density and cyclic stability of NiNT/f-CNT –NNT1510, as the cell which shows the highest performance among other samples, have been investigated.

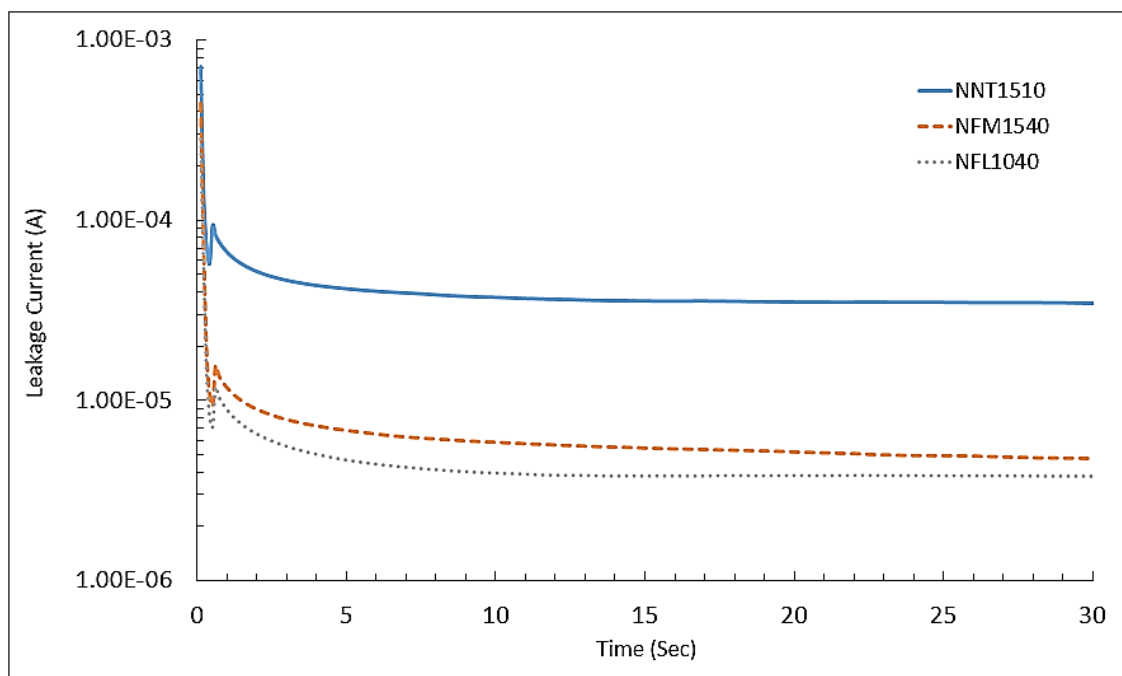


Figure 28. Leakage current test results for NNT1510, NFM1540 and NFL1040.

6. Galvanostat Charge-Discharge, Energy and Power Density, and Cyclic Stability

Cyclic charge and discharge test was done for NNT1510, with currents of 0.5mA, 1mA, 1.5mA, 2mA and 2.5mA (Fig.29.A). The charge-discharge curves are nearly linear and symmetrical, which represents a close electrochemical behavior of NNT1510 to an ideal supercapacitor (Fig.29.B). The Ragone plot of the NiNT/f-CNT supercapacitor is generated from discharge curves and shown in Fig.29.C. The highest power density of 81 kW/kg occurs at an energy density of 14.6 Wh/kg.

NNT1510 demonstrates an acceptable cyclic stability: the capacitance retained 90 % of its original value after 1000 cycles at the scanning rate of 50 mV/sec, (Fig.29.D). Considering that the NiNT/f-CNT electrode is a binder-free electrode, the loss of capacity could be due to continuous discharge of f-CNT to the electrolyte during cyclic charge and discharge. To confirm the present of pure carbon on NiNTs, thermal analysis has been done.

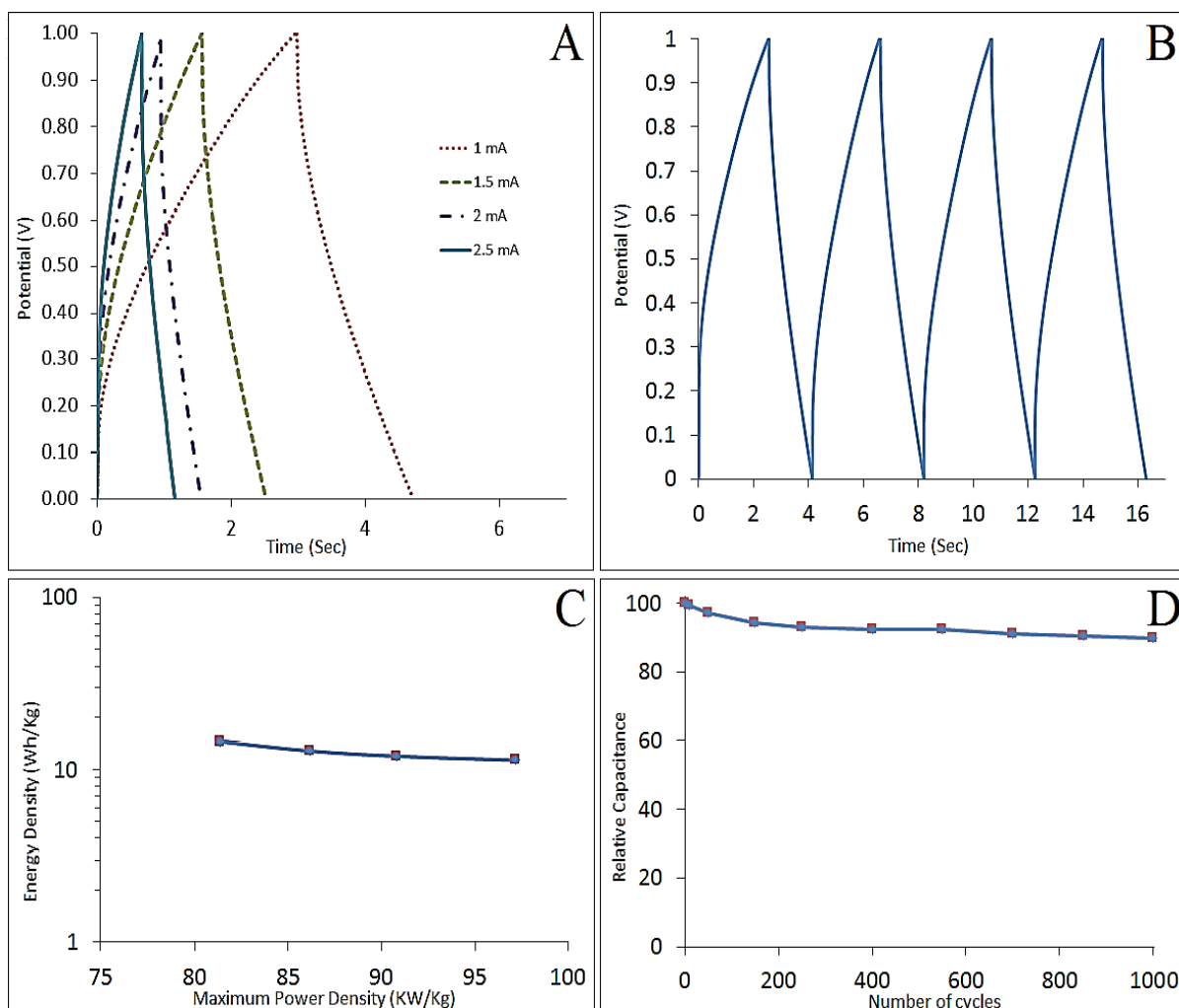


Figure 29. A) CCD curves of NNT1510 at different current densities, B) Four cycles of CCD for NNT1510 at 2.5mA, C) Ragone plot of sample NNT1510 and D) Cyclic stability of NNT1510 at scanning rate of 50 mV/Sec.

7. Combined Thermal Analysis and Fourier Transform Infrared Spectroscopy (FT-IR)

The TGA was coupled with an infrared (IR) spectroscopy (Bruker Tensor 37) to identify gasses eluted during the heating process. The TGA signal (% mass) and Gram-Schmidt signal (IR absorbance intensity) were plotted in Fig.30. As can be seen in Fig.30, the Gram-Schmidt signal starts to change at 270°C and reach a peak at 390°C, a sign of gas evolution from the sample.

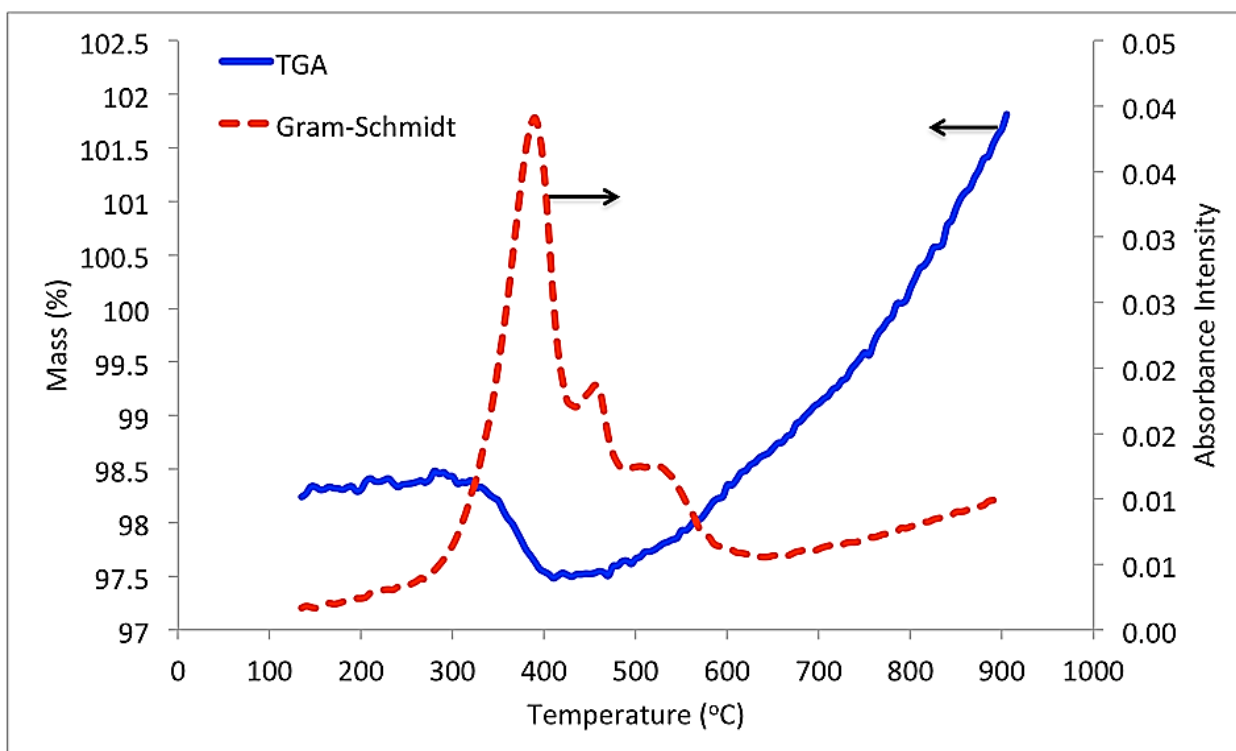


Figure 30. Combined thermogravimetric analysis and FT-IR Spectroscopy of NNT1510.

IR absorbance spectrum at the Gram-Schmidt peak was identified as carbon dioxide by comparing it with the gas library in the OPUS software (Fig.31). Since f-CNTs are the only carbon source in the sample, the eluted CO_2 must come from the oxidization of f-CNTs. At the same temperature range of 270-390°C, the TGA signal shows a step decrease of sample mass of 0.75% (or 0.034mg consider initial sample mass of 4.5mg). The previous study on oxidization of nickel nanowire during thermal annealing shows that no oxidation of the nickel nanowire can happen at a temperature lower than 400°C. [62] As a result, the step change of sample mass below 400°C can only be caused by the oxidation of f-CNT to CO_2 . In other words, the 0.034 mg mass loss is the mass of f-CNTs on the NNT1510 sample. This value is well comparable with the value of f-CNT mass obtained from the high-resolution analytical scale (0.032 mg).

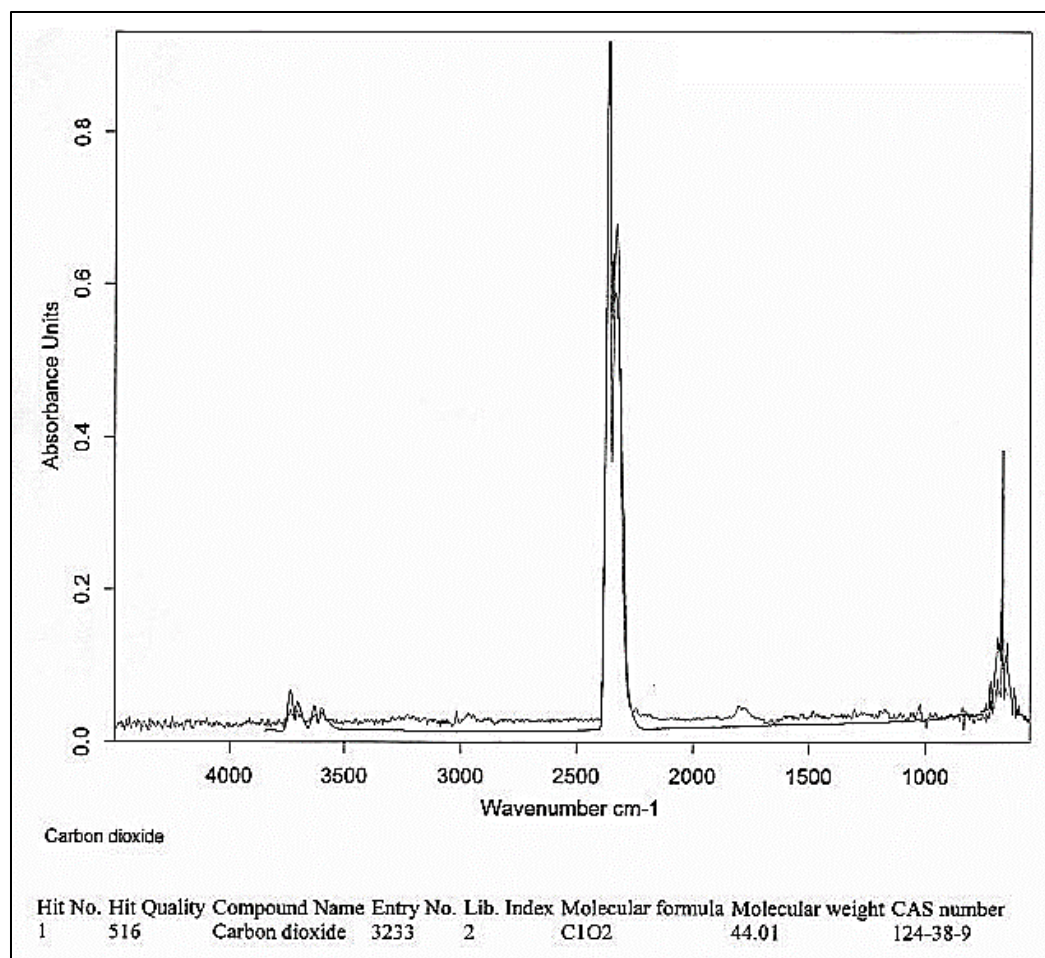


Figure 31. IR gas analysis of NNT1510.

CHAPTER IV: SUMMARY AND CONCLUSIONS

Electrophoretic deposition was used to fabricate f-CNT-based supercapacitor electrodes with macro, micro and nanostructured current collectors. Morphology study of the cells confirms that constant current EPD can provide a conformal coating of CNTs wrapping around nickel nanotubes, build a uniform f-CNT layer on nickel foam without blocking pores of the substrate and make a uniform layer of f-CNTs on the surface of the nickel plate. It is critical to control EPD time and current to reach the final morphology of CNT coating which affects the cell performance. For example, in the case of NiNT/f-CNT cells, EPD fills the voids in the nanostructured current collector with f-CNT and produce a conformal coating of f-CNT onto the surface of the nanostructure. Prolonged deposition time at high current, however, will result in f-CNTs sitting on top of the nanostructure, which has negative effective on the rate capability.

The rate capability of the f-CNT electrode is improved by introducing nanostructured interface between f-CNT and nickel current collector for taking advantages of using electrically conductive 3D current collectors. The electrochemical performance of the cells confirms that using a 3D nano-structure current collector will increase the rate capability of the nickel-CNT cells up to 51% in the scanning rate range of 1 to 50 mV/sec. Moreover, EIS analysis shows using 3D current collector decreases dielectric relaxation time and ESR which increases the rate capability subsequently. EIS test also demonstrates the highest leakage current resistance of 5730 Ω for NiNT/f-CNT cell, which is another benefit of using 3D current

collector for supercapacitors. The integrated device of NiNT/f-CNT shows a specific capacitance of 200 F/g for the electrode material and up to 90% cycle stability after 1000 cycles. Maximum power energy of 81 kW/kg was obtained at the energy density of 14.6 Wh/kg for NiNT/f-CNT cell. The developed EPD can be applied to deposit charged nano-particles onto any conductive substrate to create working electrodes. For example, it can be used to deposit functionalized graphene onto a nanostructured current collector to afford even better supercapacitance performance.

REFERENCES

- [1]. B. Conway, *Electrochemical supercapacitors: scientific fundamentals and technological applications*, Springer Science & Business Media, 2013.
- [2]. P. Sharma, and T. S. Bhatti. "A review on electrochemical double-layer capacitors." *Energy Conversion and Management* 51, no. 12 (2010): 2901-2912.
- [3]. R. Kötz, and M. Carlen. "Principles and applications of electrochemical capacitors." *Electrochimica acta* 45, no. 15 (2000): 2483-2498.
- [4]. Augustyn, Veronica, Patrice Simon, and Bruce Dunn. "Pseudocapacitive oxide materials for high-rate electrochemical energy storage." *Energy & Environmental Science* 7, no. 5 (2014): 1597-1614.
- [5]. H. Tang, J. Wang, H. Yin, H. Zhao, D. Wang, and Z. Tang. "Growth of Polypyrrole Ultrathin Films on MoS₂ Monolayers as High-Performance Supercapacitor Electrodes." *Advanced Materials* (2014).
- [6]. P. T. Kissinger, and W. R. Heineman. "Cyclic voltammetry." *J. Chem. Educ* 60, no. 9 (1983): 702.
- [7]. R. S. Nicholson. "Theory and Application of Cyclic Voltammetry for Measurement of Electrode Reaction Kinetics." *Analytical Chemistry* 37, no. 11 (1965): 1351-1355.

- [8]. D. H. Evans, K. M. O'Connell, R. A. Petersen, and M. J. Kelly. "Cyclic voltammetry." *J. Chem. Educ* 60, no. 4 (1983): 290.
- [9]. J. Heinze. "Cyclic voltammetry—electrochemical spectroscopy". *New analytical methods (25)*. *Angewandte Chemie International Edition in English* 23, no. 11 (1984): 831-847.
- [10]. M. E. Orazem, and B. Tribollet. *Electrochemical impedance spectroscopy*. Vol. 48. John Wiley & Sons, 2011.
- [11]. A. Lasia. "Electrochemical impedance spectroscopy and its applications." In *Modern aspects of electrochemistry*, pp. 143-248. Springer US, 2002.
- [12]. B. Y. Chang, and S. M. Park. "Electrochemical impedance spectroscopy." *Annual Review of Analytical Chemistry* 3 (2010): 207-229.
- [13]. Utz. Retter, and H. Lohse. "Electrochemical impedance spectroscopy." In *Electroanalytical Methods*, pp. 149-166. Springer Berlin Heidelberg, 2005.
- [14]. P. L. Bonora, F. Deflorian, and L. Fedrizzi. "Electrochemical impedance spectroscopy as a tool for investigating under paint corrosion." *Electrochimica Acta* 41, no. 7 (1996): 1073-1082.
- [15]. P. L. Taberna, P. Simon, and J. F. Fauvarque. "Electrochemical characteristics and impedance spectroscopy studies of carbon-carbon supercapacitors." *Journal of the Electrochemical Society* 150, no. 3 (2003): A292-A300.

- [16]. S. Yoon, J. Lee, T. Hyeon, and S. M. Oh. "Electric double-layer capacitor performance of a new mesoporous carbon." *Journal of the Electrochemical Society* 147, no. 7 (2000): 2507-2512.
- [17]. D. Zhang, B. S. Haran, A. Durairajan, R. E. White, Y. Podrazhansky, and B. N. Popov. "Studies on capacity fade of lithium-ion batteries." *Journal of Power Sources* 91, no. 2 (2000): 122-129.
- [18] Instruments, Gamry. "Electrochemical Capacitors: Part 2 — Cyclic Charge Discharge and Stacks " *Applied Notes* (2014).
- [19]. B. W. Ricketts, and C. Ton-That. "Self-discharge of carbon-based supercapacitors with organic electrolytes." *Journal of Power Sources* 89, no. 1 (2000): 64-69.
- [20]. L. A. Zheng, and E. X. Ping. "Method and structure for reducing leakage current in capacitors." U.S. Patent 6,943,078, issued September 13, 2005.
- [21]. Y. Lin, S. Taylor, H. Li, K. S. Fernando, L. Qu, W. Wang, L. Gu, B. Zhou, and Y. P. Sun. "Advances toward bio applications of carbon nanotubes." *Journal of Materials Chemistry* 14, no. 4 (2004): 527-541.
- [22]. V. N. Popov. "Carbon nanotubes: properties and application." *Materials Science and Engineering: R: Reports* 43, no. 3 (2004): 61-102.
- [23]. N. Yang, X. Chen, T. Ren, P. Zhang, and D. Yang. "Carbon nanotube based biosensors." *Sensors and Actuators B: Chemical* 207 (2015): 690-715.

- [24]. S. Sotiropoulou and N. A. Chaniotakis. "Carbon nanotube array-based biosensor." *Analytical and Bioanalytical Chemistry* 375, no. 1 (2003): 103-105.
- [25]. W. Lu, L. Dai, Carbon nanotube supercapacitors, INTECH Open Access Publisher, 2010.
- [26]. E. Frackowiak. "Supercapacitor electrodes from multi-walled carbon nanotubes." *Appl. Phys. Lett.* 77.15 (2000) 2421-2423.
- [27]. A. Izadi Najafabadi, Y. Satoshi, K. Kobashi, T. Yamada, D. N. Futaba, H. Hatori, M. Yumura, S. Iijima, K. Hata. "Extracting the Full Potential of Single-Walled Carbon Nanotubes as Durable Supercapacitor Electrodes Operable at 4 V with High Power and Energy Density." *Adv. Mater.* 22.35 (2010) E235-E241.
- [28]. X. Xiao, T. Li, Z. Peng, H. Jin, Q. Zhong, Q. Hu, B. Yao. "Freestanding functionalized carbon nanotube-based electrode for solid-state asymmetric supercapacitors." *Nano Energy* 6 (2014) 1-9.
- [29]. S. He, H. Hou, W. Chen. "3D porous and ultralight carbon hybrid nanostructure fabricated from carbon foam covered by monolayer of nitrogen-doped carbon nanotubes for high performance supercapacitors." *J. Power Sources* 280 (2015) 678-686.
- [30]. H. Liu, H. Song, X. Chen, S. Zhang, J. Zhou, Z. Ma. "Effects of nitrogen-and oxygen-containing functional groups of activated carbon nanotubes on the electrochemical performance in supercapacitors." *J. Power Sources* 285 (2015) 303-309.

- [31]. M. Sun, G. Wang, X. Li, C. Li. "Irradiation preparation of reduced graphene oxide/carbon nanotube composites for high-performance supercapacitors." *J. Power Sources* 245 (2014) 436-444.
- [32]. N. Jha, P. Ramesh, E. Bekyarova, M. E. Itkis, R. C. Haddon. "High energy density supercapacitor based on a hybrid carbon nanotube–reduced graphite oxide architecture." *Adv. Energy Mater.* 2.4, (2012) 438-444.
- [33]. Z. Zhu, Y. Hu, H. Jiang, C. Li. "A three-dimensional ordered mesoporous carbon/carbon nanotubes nanocomposites for supercapacitors." *J. Power Sources* 246 (2014) 402-408.
- [34]. Q. Mahmood, H. Joong Yun, W. S. Kim, H. S. Park. "Highly uniform deposition of MoO₃ nano-dots on multi-walled carbon nanotubes for improved performance of supercapacitors." *J. Power Sources* 235 (2013) 187-192.
- [35]. Z. Zhang, W. Wang, C. Li, L. Wei, X. Chen, Y. Tong, K. Mai, and X. Lu. "Highly conductive ethylene–vinyl acetate copolymer/carbon nanotube paper for lightweight and flexible supercapacitors." *J. Power Sources* 248 (2014) 1248-1255.
- [36]. Y. J. Peng, T. H. Wu, C. T. Hsu, S. M. Li, M. G. Chen, C. C. Hu. "Electrochemical characteristics of the reduced graphene oxide/carbon nanotube/polypyrrole composites for aqueous asymmetric supercapacitors." *J. Power Sources* 272 (2014) 970-978.
- [37]. H. Yi, H. Wang, Y. Jing, T. Peng, X. Wang. "Asymmetric supercapacitors based on carbon nanotubes@ NiO ultrathin nanosheets core-shell composites and MOF-derived porous carbon polyhedrons with super-long cycle life." *J. Power Sources* 285 (2015) 281-290.

- [38]. C. Choi, J. A. Lee, A. Y. Choi, Y. T. Kim, X. Lepró, M. D. Lima, R. H. Baughman, S. J. Kim. "Flexible supercapacitor made of carbon nanotube yarn with internal pores." *Advanced Materials* 26, no. 13 (2014): 2059-2065.
- [39]. R. A. Fisher, M. R. Watt, R. Konjeti, W. J. Ready. "Atomic Layer Deposition of Titanium Oxide for Pseudocapacitive Functionalization of Vertically-Aligned Carbon Nanotube Supercapacitor Electrodes." *ECS J. Solid State Sci. Technol.* 4.2 (2015) M1-M5.
- [40]. T. Wang, D. Song, H. Zhao, J. Chen, C. Zhao, L. Chen, W. Chen, J. Zhou, E. Xie. "Facilitated transport channels in carbon nanotube/carbon nanofiber hierarchical composites decorated with manganese dioxide for flexible supercapacitors." *J. Power Sources* 274 (2015) 709-717.
- [41]. H. Liu, H. Song, X. Chen, S. Zhang, J. Zhou, Z. Ma. "Effects of nitrogen-and oxygen-containing functional groups of activated carbon nanotubes on the electrochemical performance in supercapacitors." *J. Power Sources* 285 (2015) 303-309.
- [42]. H. Zheng, J. Wang, Y. Jia. "In-situ synthesize multi-walled carbon nanotubes@ MnO₂ nanoflake core-shell structured materials for supercapacitors." *J. Power Sources* 216 (2012) 508-514.
- [43]. H. Fang, S. Zhang, X. Wu, W. Liu, B. Wen, Z. Du, T. Jiang. "Facile fabrication of multiwalled carbon nanotube/ α -MnOOH coaxial nanocable films by electrophoretic deposition for supercapacitors." *J. Power Sources* 235 (2013) 95-104.

- [44]. M. A. Bavio, G. G. Acosta, T. Kessler. "Synthesis and characterization of polyaniline and polyaniline–carbon nanotubes nanostructures for electrochemical supercapacitors." *J. Power Sources* 245 (2014) 475-481.
- [45]. Y. Su, I. Zhitomirsky. "Hybrid MnO_2 /carbon nanotube-VN/carbon nanotube supercapacitors." *J. Power Sources* 267 (2014) 235-242.
- [46]. A. H. P. de Oliveira, and H. P. de Oliveira. "Carbon nanotube/polypyrrole nanofibers core–shell composites decorated with titanium dioxide nanoparticles for supercapacitor electrodes." *J. Power Sources* 268 (2014) 45-49.
- [47]. M. Huang, R. Mi, H. Liu, F. Li, X. L. Zhao, W. Zhang, S.X. He, Y.X. Zhang. "Layered manganese oxides-decorated and nickel foam-supported carbon nanotubes as advanced binder-free supercapacitor electrodes." *J. Power Sources* 269 (2014) 760-767.
- [48]. Y. J. Peng, T. H. Wu, C. T. Hsu, S. M. Li, M. G. Chen, and C. C. Hu. "Electrochemical characteristics of the reduced graphene oxide/carbon nanotube/polypyrrole composites for aqueous asymmetric supercapacitors." *Journal of Power Sources* 272 (2014) 970-978.
- [49]. S. He, H. Hou, and W. Chen. "3D porous and ultralight carbon hybrid nanostructure fabricated from carbon foam covered by monolayer of nitrogen-doped carbon nanotubes for high performance supercapacitors." *Journal of Power Sources* 280 (2015) 678-686.
- [50]. H. Yi, H. Wang, Y. Jing, T. Peng, and X. Wang. "Asymmetric supercapacitors based on carbon nanotubes@ NiO ultrathin nanosheets core-shell composites and MOF-derived porous carbon polyhedrons with super-long cycle life." *Journal of Power Sources* 285 (2015) 281-290.

[51]. N. Jung, S. Kwon, D. Lee, D. M. Yoon, Y. M. Park, A. Benayad, J. Y. Choi, and J. S. Park. "Synthesis of chemically bonded graphene/carbon nanotube composites and their application in large volumetric capacitance supercapacitors." *Advanced Materials* 25, no. 47 (2013) 6854-6858.

[52]. M. Beidaghi and Y. Gogotsi. "Capacitive energy storage in micro-scale devices: recent advances in design and fabrication of micro-supercapacitors." *Energy & Environmental Science* 7, no. 3 (2014) 867-884.

[53]. L. Hu, W. Chen, X. Xie, N. Liu, Y. Yang, H. Wu, Y. Yao, M. Pasta, H. N. Alshareef, and Yi Cui. "Symmetrical MnO₂-carbon nanotube-textile nanostructures for wearable pseudocapacitors with high mass loading." *Acs Nano* 5, no. 11 (2011) 8904-8913.

[54]. G. Zhu, Z. He, J. Chen, J. Zhao, X. Feng, Y. Ma, Q. Fan, L. Wang, and W. Huang. "Highly conductive three-dimensional MnO₂-carbon nanotube-graphene-Ni hybrid foam as a binder-free supercapacitor electrode." *Nanoscale* 6, no. 2 (2014) 1079-1085.

[55]. J. Ji, L. L. Zhang, H. Ji, Y. Li, X. Zhao, X. Bai, X. Fan, F. Zhang, and R. S. Ruoff. "Nanoporous Ni (OH)₂ thin film on 3D ultrathin-graphite foam for asymmetric supercapacitor." *ACS nano* 7, no. 7 (2013) 6237-6243.

[56]. A. R. Boccaccini, I. Zhitomirsky. "Application of electrophoretic and electrolytic deposition techniques in ceramics processing." *Curr. Opin. Solid State Mater. Sci.* 6.3 (2002) 251-260.

[57]. Q. Wang, and H. Moriyama. "Carbon nanotube-based thin films: synthesis and properties." INTECH Open Access Publisher, 2011.

- [58]. Y. Wang, Z. Shi, Y. Huang, Y. Ma, C. Wang, M. Chen, Y. Chen. "Supercapacitor devices based on graphene materials." *J. Phys. Chem. C* 113.30 (2009) 13103-13107.
- [59]. S.W. Lee, N. Yabuuchi, B. M. Gallant, S. Chen, B. S. Kim, P. T. Hammond, Y. Shao-Horn. "High-power lithium batteries from functionalized carbon-nanotube electrodes." *Nat. Nanotechnol.* 5.7 (2010) 531-537.
- [60]. A. R. Boccaccini, J. Cho, J. A. Roether, B. J. Thomas, E. J. Minay, M.S. Shaffer. "Electrophoretic deposition of carbon nanotubes." *Carbon* 44.15 (2006) 3149-3160.
- [61]. C. Du, N. Pan. "High power density supercapacitor electrodes of carbon nanotube films by electrophoretic deposition". *Nanotechnology* 17.21 (2006) 5314.
- [62]. Y. Ren, W. K. Chim, S. Y. Chiam, J. Q. Huang, C. Pi, J. S. Pan. "Formation of Nickel Oxide Nanotubes with Uniform Wall Thickness by Low Temperature Thermal Oxidation Through Understanding the Limiting Effect of Vacancy Diffusion and the Kirkendall Phenomenon." *Adv. Funct. Mater.* 20. 19 (2010) 3336-3342.